biomolecules

MDPI

Article

Ethacrynic Acid-Based Chalcone Derivatives Bearing Allyl and Propargyl Groups: Synthesis, Structural Characterization, Anticancer Evaluation, Molecular Docking and DFT Calculations

Hassan Harrouni [1,2,†], Garba Suleiman [1,3,†], Hanna Dib [4], Ghanem Hamdoum [1], Nabil El Brahmi [1], Gérald Guillaumet [1,2] and Saïd El Kazzouli [1,*]

[1] School of Engineering in Biomedical and Biotechnology, Euromed University of Fes (UEMF), Fes 30000, Morocco; h.harrouni@ueuromed.org (H.H.); s.garba@ueuromed.org (G.S.); g.hamdoun@ueuromed.org (G.H.); n.elbrahmi@ueuromed.org (N.E.B.); gerald.guillaumet@univ-orleans.fr (G.G.)
[2] Institut de Chimie Organique et Analytique, Université d'Orléans, UMR CNRS 7311, BP 6759, CEDEX 2, 45067 Orléans, France
[3] Department of Chemistry, Yobe State University, Damaturu 620101, Nigeria
[4] College of Engineering and Technology, American University of the Middle East, Egaila 54206, Kuwait; hanna.dib@aum.edu.kw
* Correspondence: s.elkazzouli@ueuromed.org
† These authors contributed equally to this work and share first authorship.

Abstract

A series of ethacrynic acid (**EA**)-based chalcone derivatives (**4**, **5**, **7**, **8**, **9**, **10** and **11**) incorporating propargyl or allyl ether groups were synthesized and evaluated for anticancer activity. Structural characterization confirmed successful synthesis of **EA**-based chalcone derivatives, extending the Michael acceptor system while introducing click-compatible functionality. Preliminary screening at 25 μM identified pyridine (**9**) and phenyl (**10**) derivatives as leads, with **9** showing comparable activity to roscovitine at five-fold lower concentration. Propargyl ethers consistently outperformed allyl analogs. Click chemistry conversion of **9** to triazole **11** via CuAAC yielded the most active compound, with improved activity across six cancer lines. Compound **11** exhibited enhanced activity against MDA-MB-468 and MCF7 cells (IC_{50} = 6 μM), representing 2.7-fold superiority over roscovitine, while maintaining acceptable selectivity versus fibroblasts (IC_{50} = 21 μM, SI = 3.5). In silico docking across multiple targets (1HCK, 3DDQ, 4EZ5, 3UG2, 7AAD, 1JDH) consistently prioritized compound **11**, mirroring the in vitro ranking. These findings establish that click chemistry may serve as a viable lead-optimization strategy in **EA** medicinal chemistry.

Keywords: anticancer activity; chalcone; click chemistry; DFT; ethacrynic acid; molecular docking

Academic Editor: Iogann Tolbatov

Received: 2 November 2026
Revised: 19 November 2026
Accepted: 21 November 2026
Published: 26 November 2026

Copyright: © 2026 by the authors. Licensee MDPI, Basel, Switzerland. This article is an open access article distributed under the terms and conditions of the Creative Commons Attribution (CC BY) license.

1. Introduction

Cancer remains a leading cause of mortality worldwide, accounting for nearly 10 million deaths in 2020 according to the World Health Organization [1]. The global cancer burden is projected to reach 28.4 million cases by 2040, representing a 47% increase from

2020 [2,3]. Despite significant advances in early detection and therapeutic interventions, chemoresistance continues to undermine treatment efficacy across multiple malignancies, with multidrug resistance (MDR) mechanisms contributing to approximately 90% of metastatic cancer treatment failures. This persistent challenge necessitates innovative therapeutic strategies targeting resistance pathways while maintaining acceptable safety profiles [4,5].

Within this landscape of therapeutic resistance, glutathione S-transferases (GSTs) play a central role in drug detoxification pathways [6,7]. These phase II enzymes catalyze glutathione conjugation to electrophilic xenobiotics, facilitating elimination, but their overexpression in malignant cells particularly the π-class isoform GSTP1 confers MDR by accelerating chemotherapeutic clearance [8]. Consequently, GST inhibition represents a validated strategy to potentiate conventional cytotoxicity and overcome resistance mechanisms [9].

To address the limitations of current anticancer therapies, ethacrynic acid (**EA**) has emerged as a promising scaffold for drug development [10,11]. **EA** is an FDA-approved loop diuretic characterized by its α,β-unsaturated carbonyl moiety, which functions as a Michael acceptor and enables covalent inhibition of GSTP1 through modification of active-site cysteine residues [12]. Beyond its diuretic activity, it has demonstrated cytotoxic effects across diverse cancer cell lines and has been evaluated clinically as an adjuvant to enhance standard chemotherapeutics [13]. Nevertheless, its application in oncology remains restricted by moderate potency, limited isoform selectivity, and dose-dependent diuretic effects. These limitations have prompted extensive synthetic efforts toward **EA** analogs with improved antiproliferative activity and GSTP1 inhibition [14–16].

Indeed, various structural modifications at key functional sites have proven effective. Carboxylic-group derivatization through simple amides or related analogs [12], incorporation of oxadiazole and thiazole motifs, ester formation, and sulfonamide substitution have all produced derivatives with moderate to excellent antiproliferative activity relative to unmodified **EA** [17–19]. These efforts have been further expanded through recent computational studies integrating SAR insights with mechanistic modeling [20].

Structurally diverse small-molecule scaffolds play a central role in medicinal chemistry due to their versatility and broad spectrum of biological activities [21,22]. Among these, chalcone derivatives represent a privileged and chemically versatile class that has garnered considerable attention in anticancer drug discovery [23]. Their defining α, β-unsaturated carbonyl system not only mirrors the Michael acceptor functionality of **EA** but also enables diverse modes of biological engagement, including covalent modification of nucleophilic residues and modulation of redox-sensitive pathways [24]. The extended conjugation inherent to the chalcone framework supports extensive substituent diversification, allowing precise modulation of electronic character, molecular recognition, and physicochemical properties [25]. This combination of reactivity and tunability has positioned chalcones as valuable intermediates and productive starting points for constructing pharmacologically active architectures. Although numerous **EA**-derived compounds [11] and chalcone-based anticancer agents [23] have been reported over the years, **EA** derivatives containing chalcone functionality have not been previously described to the best of our knowledge.

The present work reports the design, synthesis and anticancer evaluation of EA-based chalcone derivatives bearing propargyl or allyl ether. In addition to providing synthetic precursors for subsequent Cu(I)-catalyzed azide-alkyne cycloaddition (CuAAC) reactions, the allyl- and propargyl-substituted chalcones were designed as biologically relevant analogs to investigate the influence of terminal unsaturated substituents on antiproliferative activity. The allyl derivatives served as important comparator molecules because

they possess steric features comparable to the propargyl analogues while lacking the ability to undergo click chemistry. This design enabled preliminary structure-activity relationship (SAR) analysis and facilitated assessment of whether biological activity could be further enhanced through triazole incorporation.

The preliminary SAR investigation was intentionally focused on identifying the most promising chalcone precursor before undertaking further molecular diversification. Among the synthesized chalcone derivatives, compound **9** exhibited the most favorable biological profile and was therefore selected for CuAAC-mediated modification. The synthesis of compound **11** was designed as a proof-of-concept study to evaluate whether incorporation of a 1,2,3-triazole pharmacophore could improve antiproliferative activity. The enhanced activity observed for compound **11** validates this strategy and provides a foundation for the future development of a broader library of triazole-containing analogues.

The compounds were obtained via a Claisen–Schmidt base-catalyzed condensation between the functionalized **EA** intermediates and a series of aromatic aldehydes. The structures of the new analogs were confirmed by FTIR, ^{1}H, ^{13}C and 2D NMR spectroscopy, HRMS, and density functional theory (DFT) calculation. Their anticancer activity was first evaluated through in-vitro cytotoxicity assays against seven cancer cell lines.

Subsequent CuAAC-mediated derivatization enabled lead optimization, yielding compound **11** as the most active member of the series. This derivative, obtained from first-generation hit **9**, exhibited lower IC_{50} values and improved selectivity compared to the reference drug roscovitine. The molecular docking studies were thereafter performed to analyze the interactions responsible for their biological activity, revealing key binding features that support further investigation of these derivatives as promising anticancer agents.

2. Materials and Methods

2.1. Reagents and Instrumentation

All chemicals and reagents were sourced from commercial suppliers (Alfa Aesar (UK), Sigma Aldrich (Germany)) and used as received without additional purification. Analytical thin-layer chromatography (TLC) was conducted on silica gel 60 F254 plates (Merck, Germany), with compound visualization achieved under ultraviolet light at wavelengths of 254 or 365 nm. Silica gel 60 (230–400 mesh, particle size 0.040–0.063 mm, Merck) was used for column chromatography. Melting points were determined with samples in open capillary tubes using a BioCote Thermo Scientific digital melting point apparatus (IA9200) (UK), and the values are uncorrected. Infrared spectra were obtained using a Thermo Scientific Nicolet IS50 FT-IR spectrometer (Madison, WI 53711, USA) and are reported in wavenumbers (cm^{-1}). ^{1}H NMR and ^{13}C NMR spectra were recorded on a JEOL 600 MHz spectrometer (Japan), operating at 600 MHz for ^{1}H and 151 MHz for ^{13}C NMR, using appropriate deuterated solvents with tetramethylsilane (TMS) as internal standard. Chemical shifts are reported in parts per million (δ ppm). Signal multiplicities are described as singlet (s), doublet (d), triplet (t), quartet (q), or multiplet (m), and coupling constants (J) are given in hertz (Hz). High-resolution mass spectrometry (HRMS) analyses were performed in a positive mode on a Maxis Bruker 4G instrument (Germany) using electrospray ionization (ESI). UV-Vis spectra were recorded in DCM using solutions prepared at a concentration of 0.1 mg mL^{-1}. Measurements were carried out at room temperature using a 1 cm quartz cuvette with a UV–Vis spectrophotometer (Perkin-Elmer, Labsphere, North Sutton, NH, USA)

Synthetic Procedures

To the best of our knowledge and based on an extensive literature survey, all compounds described in the present study, including compounds **4**, **5**, **7**, **8**, **9**, **10**, and **11**, are reported herein for the first time. Their structures were established by spectroscopic techniques including FT-IR, NMR (see supplementary material Figures S1–S14), and HRMS analyses. The synthesis of intermediates **2** and **6** was carried out using protocols outlined in earlier reports with slight modifications [12].

Synthesis of 1-(4-(allyloxy)-2,3-dichlorophenyl)butan-1-one (**3**).

To a stirred solution of 2,3-dichloro-4-hydroxyacetophenone (1.0 mmol) in THF (10 mL) was added K_2CO_3 (2.0 mmol). After stirring for 15 min at rt, allyl bromide (1.2 mmol) was added dropwise. The reaction mixture was further stirred at rt and then refluxed at 55 °C for 16 h. Completion of the reaction was confirmed by TLC (hexane/EtOAc 4:1, *v*/*v*). The mixture was quenched with water (20 mL) and extracted with EtOAc (3 × 20 mL). Combined organic layers were washed with H_2O and brine, dried over $MgSO_4$, filtered, and concentrated. The crude product was purified by column chromatography (hexane/EtOAc 9:1, *v*/*v*) to afford the allyl ether intermediate **3** as a colorless viscous liquid in 75% yield. ^{1}H NMR (600 MHz, $CDCl_3$) δ 7.35 (d, *J* = 8.6, 0.6 Hz, 1H), 6.85 (d, *J* = 8.7 Hz, 1H), 6.08–5.99 (m, 1H), 5.47 (ddd, *J* = 17.3, 1.8, 1.3 Hz, 1H), 5.34 (ddd, *J* = 10.6, 1.4 Hz, 1H), 4.65 (dt, *J* = 5.1, 1.6 Hz, 2H), 2.89 (t, *J* = 7.3 Hz, 2H), 1.76–1.67 (m, 2H), 0.96 (t, *J* = 7.4 Hz, 3H). ^{13}C NMR (151 MHz, $CDCl_3$) δ 202.3, 156.9, 133.7, 131.8, 131.4, 127.6, 123.4, 118.6, 110.9, 70.1, 44.8, 18.0, 13.8. HRMS (+ESI) *m*/*z*: $[M + H]^+$ calculated for $C_{13}H_{15}Cl_2O_2$: 273.0449, found, 273.0444.

General procedure for the synthesis of EA- derivatives **4**–**5** and **7**–**10** [26].

A mixture of propargyl or allyl ether intermediate **3** or **6** (0.5 mmol), the appropriate heteroaromatic aldehyde (1.0 mmol), and NaOH (5 mmol) in MeOH (10 mL) was stirred at room temperature for 3–10 h. Reaction progress was monitored by TLC (hexane/EtOAc 3:1, *v*/*v*). Upon completion, the mixture was poured onto crushed ice, and the resulting product was collected by filtration, washed thoroughly with water, and dried. The crude product was purified by column chromatography (hexane/EtOAc) to afford the EA-based chalcone derivatives **4**–**5** and **7**–**10.**

(E)-1-(4-(Allyloxy)-2,3-dichlorophenyl)-2-(furan-2-ylmethylene)butan-1-one (**4**).

After purification by column chromatography (hexane/EtOAc 4:1, *v*/*v*), compound **4** was obtained as a semisolid. Yield: 74%. m.p: 128–130 °C. IR (neat) *ν* (cm^{-1}): 1643, 1614, 1585. ^{1}H NMR (600 MHz, $CDCl_3$) δ 7.56 (d, *J* = 1.2 Hz, 1H), 7.13 (d, *J* = 8.4 Hz, 2H), 6.88 (d, *J* = 8.5 Hz, 2H), 6.74 (s, 2H), 6.65 (d, *J* = 3.5 Hz, 2H), 6.51 (dd, *J* = 3.5, 1.8 Hz, 2H), 6.06 (ddt, *J* = 17.2, 10.4, 5.1 Hz, 2H), 5.49 (dq, *J* = 17.3, 1.6 Hz, 2H), 5.35 (dq, *J* = 10.6, 1.4 Hz, 2H), 4.66 (dt, *J* = 5.1, 1.6 Hz, 4H), 2.85 (q, *J* = 7.5 Hz, 4H), 1.17 (t, *J* = 7.5 Hz, 6H). ^{13}C NMR (151 MHz, $CDCl_3$) δ 195.9, 156.0, 151.2, 145.2, 139.9, 133.1, 132.0, 131.3, 130.7, 126.8, 123.1, 118.6, 116.6, 112.7, 111.1, 70.2, 20.0, 13.0. HRMS (+ESI) *m*/*z*: $[M + H]^+$ calculated for $C_{18}H_{18}Cl_2O_3$: 351.0555, found, 351.0549

(E)-1-(4-(Allyloxy)-2,3-dichlorophenyl)-2-((5-bromothiophen-2-yl)methylene)butan-1-one (**5**).

After purification by column chromatography (hexane/EtOAc 4:1, *v*/*v*), compound **5** was obtained as a semisolid. Yield: 56%. m.p: 132–134 °C. IR (neat) *ν* (cm^{-1}): 1647, 1603, 1585. ^{1}H NMR (600 MHz, $CDCl_3$) δ 7.11 (d, *J* = 8.5 Hz, 1H), 7.01 (d, *J* = 4.0 Hz, 1H), 6.98 (s, 1H), 6.88–6.84 (m, 2H), 6.03 (ddt, *J* = 17.2, 10.4, 5.1 Hz, 1H), 5.46 (dq, *J* = 17.2, 1.6 Hz, 1H), 5.32 (dq, *J* = 10.6, 1.4 Hz, 1H), 4.64 (dt, *J* = 5.2, 1.6 Hz, 2H), 2.74 (q, *J* = 7.5 Hz, 2H), 1.16 (t, *J* = 7.5 Hz, 3H). ^{13}C NMR (151 MHz, $CDCl_3$) δ 195.7, 156.1, 140.3, 139.7, 136.2, 133.5, 132.9, 132.0, 131.3, 130.5, 126.9, 123.1, 118.6, 118.5, 111.1, 70.2, 20.5, 12.5. HRMS (+ESI) *m*/*z*: $[M + H]^+$ calculated for $C_{18}H_{16}BrCl_2O_2S$: 444.9431, found, 444.9426.

(E)-1-(2,3-Dichloro-4-(prop-2-yn-1-yloxy)phenyl)-2-(furan-2-ylmethylene)butan-1-one (**7**).

After purification by column chromatography (hexane/EtOAc 8:1, *v*/*v*), compound **7** was obtained as a light brown solid. Yield: 84%. m.p: 126–128 °C. IR (neat) ν (cm^{-1}): 1643, 1614, 1585. ^1H NMR (600 MHz, $CDCl_3$) δ 7.56 (s, 1H), 7.17 (d, *J* = 8.5 Hz, 1H), 7.06 (d, *J* = 8.5 Hz, 1H), 6.75 (s, 1H), 6.66 (s, 1H), 6.51 (s, 1H), 4.83 (s, 2H), 2.85 (q, *J* = 7.6 Hz, 2H), 2.58 (s, 1H), 1.17 (t, *J* = 7.6 Hz, 3H). ^{13}C NMR (151 MHz, $CDCl_3$) δ 195.8, 154.9, 151.2, 145.3, 139.8, 134.0, 131.4, 130.8, 126.7, 123.3, 116.7, 112.7, 111.6, 77.0, 77.0, 57.2, 20.0, 13.1. HRMS (+ESI) *m*/*z*: $[M + H]^+$ calculated for $C_{18}H_{15}Cl_2O_3$: 349.0398, found, 349.0393.

(E)-2-((5-Bromothiophen-2-yl)methylene)-1-(2,3-dichloro-4-(prop-2-yn-1-yloxy)phenyl)butan-1-one (**8**).

After purification by column chromatography (hexane/EtOAc 4:1, *v*/*v*), compound **8** was obtained as a yellow solid. Yield 72**%.** m.p: 135–137 °C. IR (neat) ν (cm^{-1}): 3296, 2107, 1639, 1601, 1588. ^1H NMR (600 MHz, (600 MHz, $CDCl_3$) δ 7.17 (d, *J* = 8.5 Hz, 1H), 7.07 (d, *J* = 8.5 Hz, 1H), 7.04 (d, *J* = 4.0 Hz, 1H), 7.02 (s, 1H), 6.91 (d, *J* = 4.0 Hz, 1H), 4.84 (d, *J* = 2.4 Hz, 2H), 2.77 (q, *J* = 7.5 Hz, 2H), 2.59 (t, *J* = 2.4 Hz, 1H), 1.19 (t, *J* = 7.5 Hz, 3H). ^{13}C NMR (151 MHz, $CDCl_3$) δ 195.5, 155.1, 140.1, 139.7, 136.3, 133.7, 133.6, 131.4, 130.5, 126.8, 123.3, 118.6, 111.7, 77.3, 77.1, 57.2, 20.5, 12.5. HRMS (+ESI) *m*/*z*: $[M + H]^+$ calculated for $C_{18}H_{14}BrCl_2O_2S$: 442.9275, found, 442.9269.

(E)-1-(2,3-Dichloro-4-(prop-2-yn-1-yloxy)phenyl)-2-(pyridin-2-ylmethylene)butan-1-one (**9**).

After purification by column chromatography (hexane/EtOAc 4:1, *v*/*v*), compound **9** was obtained as a dark-brown sticky solid. Yield: 77%**.** m.p: 118–120 °C. IR (neat) ν (cm^{-1}): 3267, 2013, 1648, 1625, 1584. ^1H NMR (600 MHz, $CDCl_3$) δ 8.70–8.63 (m, 1H), 7.70 (td, *J* = 7.7, 1.8 Hz, 1H), 7.36 (d, *J* = 7.9 Hz, 1H), 7.25 (d, 2H), 7.22–7.19 (m, 1H), 7.07 (d, *J* = 8.5 Hz, 1H), 6.99 (s, 1H), 4.83 (d, *J* = 2.5 Hz, 2H), 2.96 (q, *J* = 7.4 Hz, 3H), 2.58 (t, *J* = 2.4 Hz, 1H), 1.21 (t, *J* = 7.4 Hz, 4H). ^{13}C NMR (151 MHz, $CDCl_3$) δ 197, 155.2, 154.6, 150.0, 146.5, 142.0, 136.4, 133.8, 131.5, 127.1, 125.6, 123.4, 123.1, 111.6, 77.3, 77.1, 57.2, 19.9, 13.3. HRMS (+ESI) *m*/*z*: $[M + H]^+$ calculated for $C_{19}H_{16}Cl_2NO_2$: 360.0558, found, 360.0553.

(E)-2-Benzylidene-1-(2,3-dichloro-4-(prop-2-yn-1-yloxy)phenyl)butan-1-one (**10**).

After purification by column chromatography (hexane/EtOAc 4:1, *v*/*v*), compound **10** was obtained as a white foam. Yield: 63%. m.p: 122–124 °C. IR (neat) ν (cm^{-1}): 3245, 2128, 1640, 1618, 1586. ^1H NMR (600 MHz, $CDCl_3$) δ 7.43–7.33 (m, 1H), 7.24 (d, *J* = 8.5 Hz, 1H), 7.09 (d, *J* = 8.5 Hz, 1H), 7.05 (s, 1H), 4.85 (d, *J* = 2.4 Hz, 1H), 2.73 (q, *J* = 7.5 Hz, 1H), 2.59 (t, *J* = 2.4 Hz, 1H), 1.25 (t, *J* = 7.5 Hz, 2H). ^{13}C NMR (151 MHz, $CDCl_3$) δ 196.7, 155.1, 143.6, 135.4, 134.1, 131.5, 129.5, 129.2, 128.7, 127.1, 123.3, 111.6, 77.3, 77.1, 57.2, 19.8, 13.5. HRMS (+ESI) *m*/*z*: $[M + H]^+$ calculated for $C_{20}H_{17}Cl_2O_2$: 359.0606, found, 359.0600.

(E)-1-(4-((1-Benzyl-1H-1,2,3-triazol-4-yl)methoxy)-2,3-dichlorophenyl)-2-(pyridin-2-ylmethylene)butan-1-one (**11**) [12].

A solution of compound **9** (0.250 mmol) and benzyl azide (0.30 mmol) in t-BuOH/H_2O (3:1 *v*/*v*, 3 mL) was treated with $CuSO_4 \cdot 5H_2O$ (0.0125 mmol) and sodium ascorbate (0.05 mmol). The reaction mixture was stirred at 60 °C overnight. Upon completion, the mixture was diluted with H_2O (20 mL) and extracted with EtOAc (2 × 20 mL). The combined organic layers were washed with brine (10 mL), dried over $MgSO_4$, filtered, and concentrated. The crude product was purified by column chromatography using hexane/EtOAc (3:1, *v*/*v*) as the eluent to afford the triazole **11** as a white solid. Yield: 80%. m.p: 115–117 °C. IR (neat) ν (cm^{-1}): 3156, 1648, 1617, 1587. ^1H NMR (600 MHz, $CDCl_3$) δ 8.66 (ddd, *J* = 4.8, 1.9, 0.9 Hz, 1H), 7.69 (td, *J* = 7.7, 1.8 Hz, 1H), 7.59 (s, 1H), 7.41–7.32 (m, 4H), 7.32–7.26 (m, 2H), 7.21 (d, *J* = 8.5 Hz, 1H), 7.11 (d, *J* = 8.6 Hz, 1H), 6.96 (s, 1H), 5.54 (s, 2H), 5.33 (s, 2H), 2.95 (q, *J* = 7.4 Hz, 2H), 1.20 (t, *J* = 7.4 Hz, 3H). ^{13}C NMR (151 MHz, $CDCl_3$) δ 197.0, 155.8, 154.6, 150.0, 146.5, 143.6, 142.0, 136.4, 134.4, 133.4, 131.4, 129.3, 129.0, 128.2,

127.4, 125.6, 123.2, 123.2, 123.1, 111.6, 63.7, 54.5, 19.9, 13.3. HRMS (+ESI) *m*/z: $[M + H]^+$ calculated for $C_{26}H_{23}Cl_2N_4O_2$: 493.1198, found, 493.1193.

2.2. Biology

Cell Culture. Skin normal fibroblastic cells were purchased from Lonza (Basel, Switzerland). Cancer cell lines were obtained from ATCC (American Type Culture Collection): HuH7 (hepatocellular carcinoma), Caco-2 (colorectal adenocarcinoma), HCT116 (colorectal carcinoma), MDA-MB-231 (triple-negative breast cancer), MDA-MB-468 (triple-negative breast cancer), MCF7 (ER-positive breast adenocarcinoma), and PC3 (prostate adenocarcinoma). Cells were grown at 37 °C in 5% CO_2 atmosphere using ATCC-recommended media: DMEM for HuH7, MDA-MB-231, MDA-MB-468, and fibroblasts; EMEM for MDA-MB-231, MDA-MB-468, MCF7, and Caco-2; McCoy's 5A for HCT116; and RPMI-1640 for PC3. All culture media were supplemented with 10% FBS, 2 mM L-glutamine, and 1% penicillin–streptomycin (final concentrations: 100 U/mL penicillin and 100 µg/mL streptomycin).

Preliminary cytotoxicity screening: Compounds were solubilized in DMSO at 10 mM concentration (stock solution) and diluted in culture medium to 25 µM final concentration. Roscovitine was tested at 125 µM. Cells were plated in 96-well plates (4000 cells/well). 24 h after seeding, cells were exposed to test compounds or vehicle control (DMSO, final concentration 0.25%). After 48 h of treatment, cells were washed with PBS and fixed in ice-cold 90% ethanol/5% acetic acid for 20 min. Nuclei were stained with Hoechst 33342 (B2261, Sigma-Aldrich). Image acquisition and analysis were performed using a Cellomics ArrayScan VTI/HCS Reader (ThermoScientific). Cell survival percentages were calculated as the percentage of cell number after compound treatment relative to DMSO-treated controls. Data represent mean values from triplicate wells.

IC_{50} Determination: For dose–response studies, compounds were tested at six concentrations (0.1, 0.3, 0.9, 3, 9, 25 µM) prepared by serial dilution from 10 mM DMSO stock solutions. Cells were plated in 96-well plates (4000 cells/well) and treated 24 h post-seeding. After 48 h of compound exposure, cells were processed as described above for preliminary screening. Cell survival percentages were calculated relative to DMSO-treated controls. IC_{50} values were determined using curve fitting with XLfit 5.5.0.5 (IDBS) integrated into Microsoft Excel. The four-parameter logistic model (sigmoidal dose–response model) was applied: Y = A + ((B − A)/(1 + ((C/X)^D))), where Y is the survival percentage, X is the compound concentration, A is the minimum response, B is the maximum response, C is the IC_{50}, and D is the Hill slope. Data are reported as mean IC_{50} values from three independent experiments. Selectivity indices (SI) were calculated as the ratio of IC_{50} (normal fibroblasts) to IC_{50} (cancer cell line).

2.3. Computational Details

2.3.1. Molecular Docking

Docking was performed on compounds **7**, **9**, **10** and **11**, which were biologically active in the experimental assays. Compound **8**, the only compound that was essentially inactive, was not included in the docking study and was investigated by DFT only (Section 2.3.3).

Molecular docking was carried out in MOE 2022.02 (Chemical Computing Group) to compare the binding propensities of compounds **7**, **9**, **10** and **11** across the selected targets (PDB IDs: 1HCK, 3DDQ, 4EZ5, 1JDH, 7AAD and 3UG2). Protein structures were prepared by removing crystallographic waters except those mediating key ligand interactions, adding hydrogens, assigning protonation states, and performing a restrained energy minimization using the default MOE force field settings. (This MOE-based preparation/docking approach follows our previously validated workflow reported in [27].

The agreement between experimental and re-docked poses was evaluated by RMSD, yielding values of 1.07–2.15 Å across the validated structures, indicating acceptable reproduction of the crystallographic binding modes. For PDB 1JDH, which lacks a co-crystallized ligand in the relevant pocket, the binding site was defined manually (site selection) and the resulting poses were treated as qualitative hypotheses.

Ligands were prepared by geometry optimization and conformational sampling prior to docking. Docking was performed using the standard MOE placement and scoring workflow (placement, rescoring, and refinement), and the top-ranked pose(s) were retained for interaction analysis and figure generation.

2.3.2. ADME, Drug-likeness, and Toxicity Prediction

Because docking score alone is not sufficient to evaluate a compound's potential as a drug candidate, an in-silico drug-likeness and pharmacokinetic assessment was performed. Drug-likeness and key ADME-related descriptors were predicted using SwissADME (http://www.swissadme.ch/, accessed on 1 November 2026), including water solubility (ESOL LogS), gastrointestinal (GI) absorption, blood–brain barrier (BBB) permeability, CYP1A2 inhibition, CYP3A4 inhibition, and compliance with Lipinski's rule of five and Veber criteria [28]. To complement these predictions with pharmacokinetic disposition parameters, volume of distribution (VDss, L/kg) and total clearance (mL/min/kg) were estimated using the ADMETlab 3.0/ADMETmesh evaluation platform [29]. These parameters were used to compare the expected systemic distribution and elimination tendencies of the investigated compounds. For toxicity profiling, the compounds were further evaluated using ProTox-II (http://tox.charite.de/protox_II/, accessed on 1 November 2026), which was used to predict acute oral toxicity (LD_{50}) and major toxicity endpoints, including hepatotoxicity, carcinogenicity, and mutagenicity [30].

2.3.3. DFT

For the DFT calculations, we selected compounds **8** and **11**. Compound **8**, which was essentially inactive in the biological assays and therefore excluded from the docking study (Section 2.3.1), was chosen for stereochemical investigation of its double bond. The 5-bromothiophene group at the double bond also makes it well suited to NMR analysis, which can be used to verify the double-bond stereochemistry and to support the DFT results. Compound **11** was included in both the docking and DFT analyses because of its significant biological activity.

DFT calculations were carried out using the Gaussian 09 software package. The molecular geometries of compounds **8** and **11** were optimized at the B3LYP/6-311G level of theory in the gas phase, considering the neutral singlet ground state (charge = 0, multiplicity = 1). Harmonic vibrational frequency calculations were performed at the same level of theory to confirm that each optimized structure is a true minimum on the potential energy surface (no imaginary frequencies). The optimized structures were then used to compute the frontier molecular orbital energies (HOMO and LUMO), the HOMO-LUMO energy gap, the dipole moment, the polarizability, and the thermodynamic parameters.

2.4. NMR

GEMSTONE-selective NOESY experiments. Selective 1D NOESY experiments were performed on a JEOL ECZ 600 MHz NMR spectrometer using the GEMSTONE approach to investigate the spatial proximities between selected protons of compound **8**. Selective excitation was achieved using a frequency-swept CHIRP pulse with a duration of 70 ms, a sweep bandwidth of 2.5 kHz, and 10% smoothing. The pulse sequence employed bipolar rectangular gradient pulses with a duration of 70 ms and amplitudes of 2.2 and −2.2 mT m^{-1}. The NOESY mixing time was set to 2 s, with a relaxation delay of 2 s. Spectra were

acquired using 16 scans, with 8 prescans. The selective excitation frequency was adjusted to target H1, H18, or H11, allowing the corresponding NOE correlations to be investigated within the congested aromatic region (δ 6.86–7.18 ppm).

2D NMR experiments. The 1H-1H COSY and NOESY experiments were performed on a JEOL ECZ 600 MHz NMR spectrometer. The COSY experiment was used to establish proton–proton coupling networks, while the NOESY experiment was acquired with a mixing time of 1 s, a relaxation delay of 1.5 s, a spectral width of 15 ppm, and 4 scans.

3. Results and Discussion

3.1. Design Strategy

3.1.1. Design Rationale and Molecular Hybridization Strategy

The molecular design of the new **EA** derivatives followed a stepwise strategy beginning with functionalization of the **EA** precursor, 1-(2,3-dichloro-4-hydroxyphenyl)butan-1-one (Figure 1). In the first stage, propargyl or allyl ether substituents were introduced at the 4-position to generate versatile intermediates suitable for CuAAC click chemistry and future probe elaboration. In the second stage, chalcone units were introduced via base-catalyzed Claisen–Schmidt condensation of the O-alkylated intermediates with aromatic aldehydes, thereby generating an extended α,β-unsaturated carbonyl system with Michael acceptor functionality. Systematic variation of the chalcone aromatic terminus (furan, bromothiophene, pyridine, phenyl) enabled evaluation of heteroatom and electronic effects on electrophilicity and reactivity [31]. These sequential transformations yielded a scaffold integrating click-ready alkyne derivatives with electronically tunable chalcone extensions, representing a novel direction compared to earlier carboxylate-focused **EA** derivatization strategies [13]. The design also supports a combined in vitro–in silico framework, integrating antiproliferative screening with molecular docking and electronic-structure analyses to rationalize reactivity patterns and identify structural determinants associated with the improved activity of the **EA**-based chalcone derivatives.

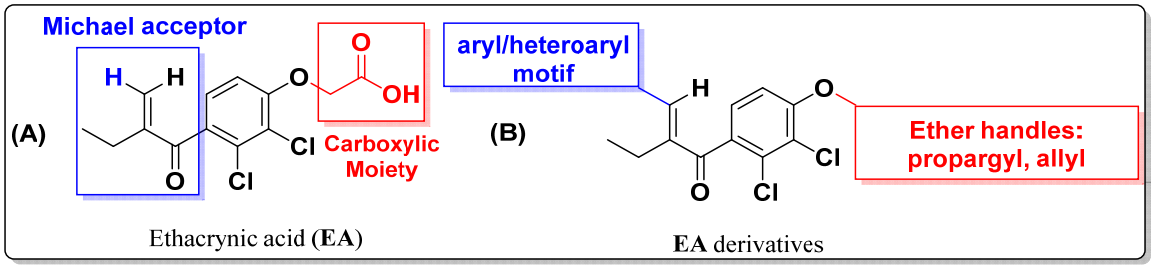


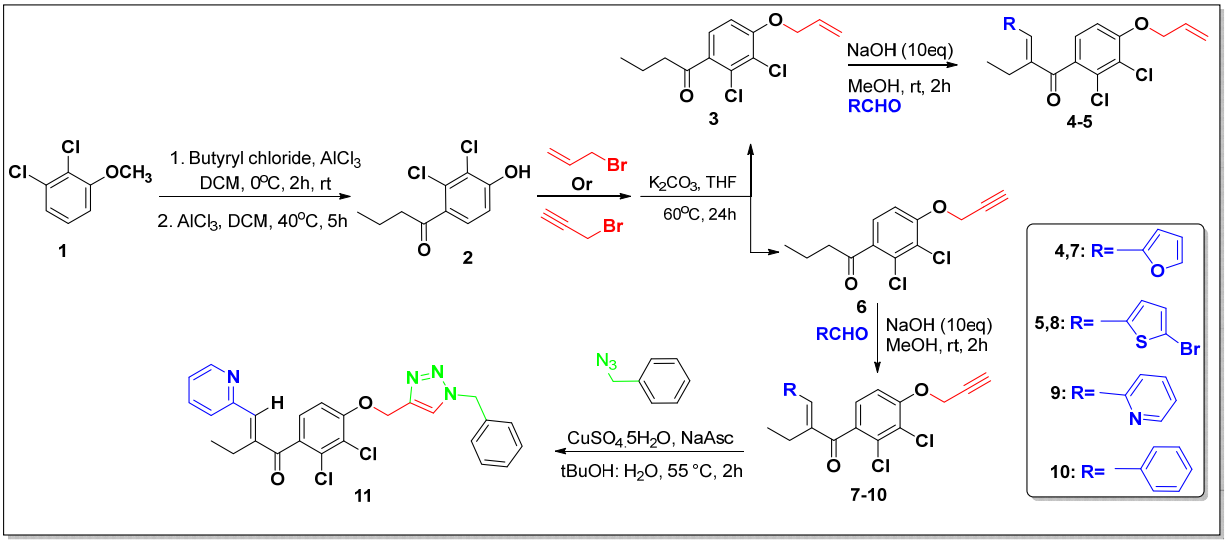
Figure 1. Design rationale for **EA**-based chalcone derivatives with O-allyl/propargyl handles. (**A**) Structure of **EA** showing the Michael acceptor pharmacophore (blue) and the carboxylic moiety (red). (**B**) Chalcone extension strategy introducing extended π-conjugation and heteroaromatic diversity (blue) coupled with the integration of propargyl/allyl ether handles at the 4-position for click chemistry applications (red).

3.1.2. Synthesis

A practical synthesis of compounds **4**–**5** and **7**–**11** was accomplished through the multistep pathway outlined in Scheme 1. Compounds **2**, **3** and **6** were prepared following previously reported procedures, with slight modifications [12]. Initially, compound **1** was subjected to treatment with butyryl chloride and aluminum chloride ($AlCl_3$) in anhydrous dichloromethane (DCM) at 0 °C for a period of 2 h. Following that, it was treated with $AlCl_3$ again under reflux for 5 h, resulting in the production of phenolic intermediate **2**

with a moderate yield. Then, the ether intermediates **3** and **6** were synthesized via O-alkylation using propargyl bromide or allyl bromide in THF, with potassium carbonate (K_2CO_3) serving as the base.

In the next step, Claisen-Schmidt condensation of intermediates **3** and **6** with selected aromatic aldehydes in methanol (MeOH) in the presence of sodium hydroxide (NaOH) at room temperature yielded the **EA**-based chalcones **4–5** and **7–10** in moderate to good yields. Finally, compound **9** was further functionalized via a CuAAC reaction with benzyl azide using $CuSO_4$/sodium ascorbate (NaAsc) in a t-BuOH/H_2O mixture, affording the corresponding triazole derivative **11** in a very good yield [12]. This modification demonstrated the propargyl substituent's versatility as a click-ready handle, allowing the addition of a triazole moiety that is known to improve hydrogen-bonding ability and metabolic stability. All compounds were characterized by ^{1}H NMR, ^{13}C NMR, IR, and HRMS (see experimental section).



Scheme 1. Synthetic route to EA-based chalcone derivatives **4–5**, **7–10** and **11**.

3.1.3. Structural Characterization

Infrared Spectroscopy

Infrared (IR) spectroscopy was employed to confirm the structural features of the synthesized **EA**-based chalcone derivatives. In all spectra, a strong absorption band corresponding to the conjugated carbonyl group ($\upsilon_{C=O}$) of the α,β-unsaturated system was observed in the range 1655–1635 cm^{-1}, consistent with chalcone formation. The associated C=C stretching vibration of the enone moiety appeared as a distinct band between 1620 and 1580 cm^{-1}. In compounds bearing a terminal alkyne group, such as **7–10**, a sharp absorption band attributable to the ≡C–H stretching vibration was detected in the region 3300–3240 cm^{-1}, accompanied by a weak C≡C stretching band near 2130–2080 cm^{-1}. As expected, these features were absent or significantly diminished in compounds lacking terminal alkynes, such as the allyl derivatives **4** and **5**. For allyl-containing derivatives, =C–H stretching bands were observed just above 3000 cm^{-1}, together with a C=C stretching vibration in the 1625–1595 cm^{-1} region, which partially overlapped with the chalcone enone absorption. In the triazole-containing derivative **11**, the disappearance of the terminal ≡C–H stretching band in the 3300–3240 cm^{-1} region, and C≡C stretching band near 2130–2080 cm^{-1} along with appearance of additional absorptions in the 1470–1380 cm^{-1} region, further confirmed successful triazole ring formation and was consistent with heterocyclic ring vibrations (Figure 2).

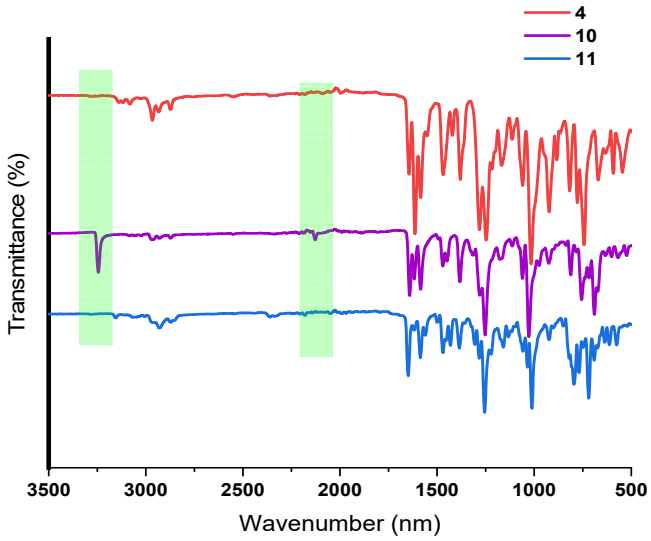


Figure 2. IR spectra of **EA**-based analogs containing allyl (**4**), propargyl (**10**) and triazole (**11**) moieties.

UV-Visible

The UV-Vis absorption spectra of compounds **4**, **5**, **7**–**11** were recorded in the range 240–360 nm (Figure 3). Compounds **4** and **5**, bearing allyloxy groups with furan and bromothiophene substituents respectively, display absorption maxima at approximately 315 nm and 325 nm. The bathochromic shift observed in compound **5** compared to compound **4** reflects the enhanced electron-donating character of the bromothiophene heterocycle relative to furan.

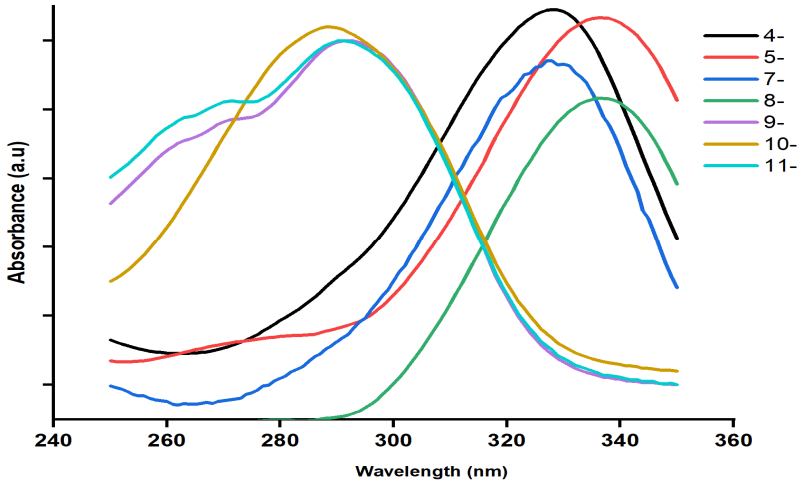


Figure 3. UV-vis spectra of compounds **4**, **5**, **7**, **8**, **9**, **10** and **11** at 250–350 nm.

Upon replacement of the allyloxy group with a propargyl-oxy group, distinct spectral changes are observed. Compound **7** (propargyl-furan derivative) exhibits a broad absorption profile spanning from 280 nm to beyond 320 nm, while compound **8** (propargyl-bromothiophene derivative) shows absorption centered at 310 nm. The broader absorption profile of compound **7** and the altered spectral pattern of compound **8** compared to their allyloxy counterparts (**4** and **5**) are attributed to the terminal alkyne functionality of

the propargyl group, which modulates the overall electronic conjugation differently than the allyl group.

Compounds **9**, **10**, and **11** exhibit absorption maxima in the 270–280 nm region. Compound **9** (pyridine derivative) and compound **10** (benzylidene derivative) display overlapping absorption around 270–280 nm. Compound **11**, the click chemistry product containing the 1,2,3-triazole linker, also absorbs primarily at 270–280 nm.

NMR Spectral Analysis

An NMR study was carried out to confirm the structures of all the synthesized compounds; however, for illustrative purposes, one terminal alkyne-containing derivative (compound **8**) and the click chemistry-derived triazole (**11**) were presented. The ^{1}H NMR spectrum of **8** showed multiple resonances between δ 7.18–6.91 ppm attributable to aromatic protons. A distinct signal at δ 4.84 ppm (2H, doublet) was assigned to a methylene group adjacent to oxygen, confirming the presence of an O–CH_2 fragment. The quartet at δ 2.77 ppm (2H) together with the triplet at δ 1.19 ppm (3H) defined an ethyl substituent. Importantly, the triplet at δ 2.59 ppm (1H) was diagnostic of a terminal alkyne proton, influenced by short-range coupling from the neighboring methylene group (Figure 4).

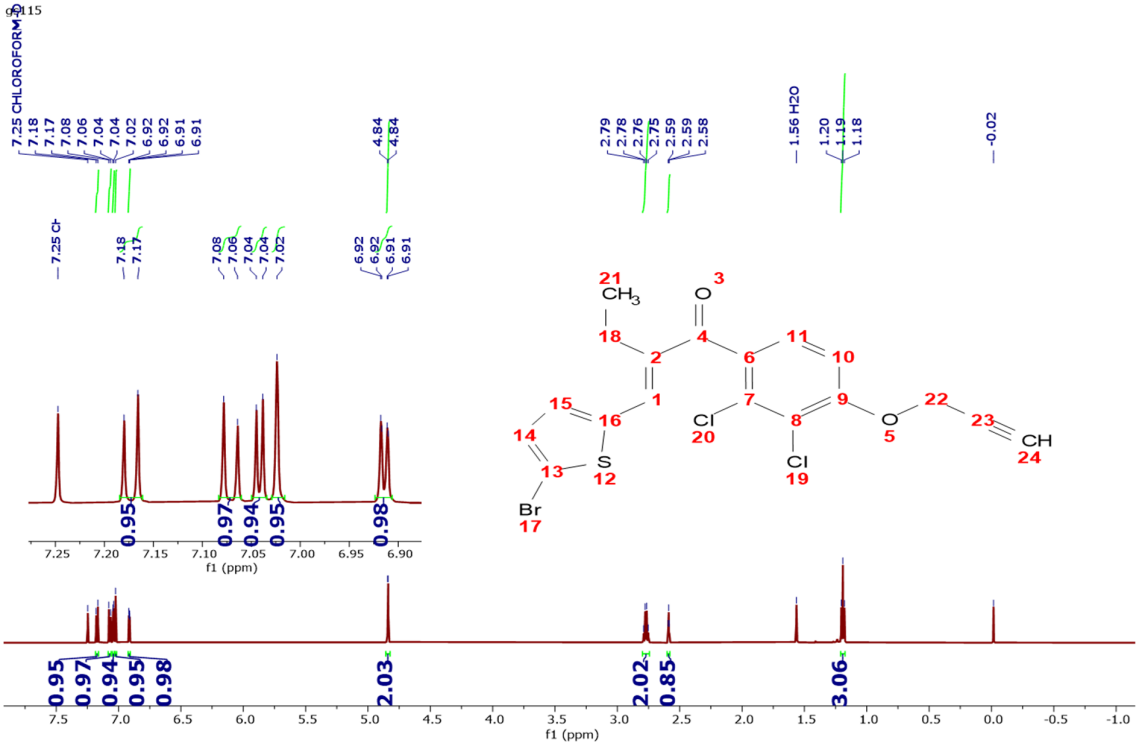


Figure 4. ^{1}H NMR (600 MHz, $CDCl_3$) spectrum of compound **8**.

In the ^{13}C NMR spectrum of **8**, a strong resonance at δ 195.5 ppm confirmed the presence of a conjugated carbonyl carbon. Signals observed in the range of δ 155.0–111.6 ppm were assigned to aromatic carbons, consistent with a substituted aryl framework. The deuterated chloroform signal appeared in the region of δ 77.3–76.9 ppm; however, two of the acetylenic carbons were observed as an overlapping resonance at δ 77.3 ppm and 77.0 ppm, Additionally, the resonance at δ 57.2 ppm was attributed to a methylene carbon adjacent to oxygen, supporting the presence of an O-CH_2 fragment, whereas the signals at δ 20.5 and 12.47 ppm corresponded to the carbons of the ethyl group (Figure 5).

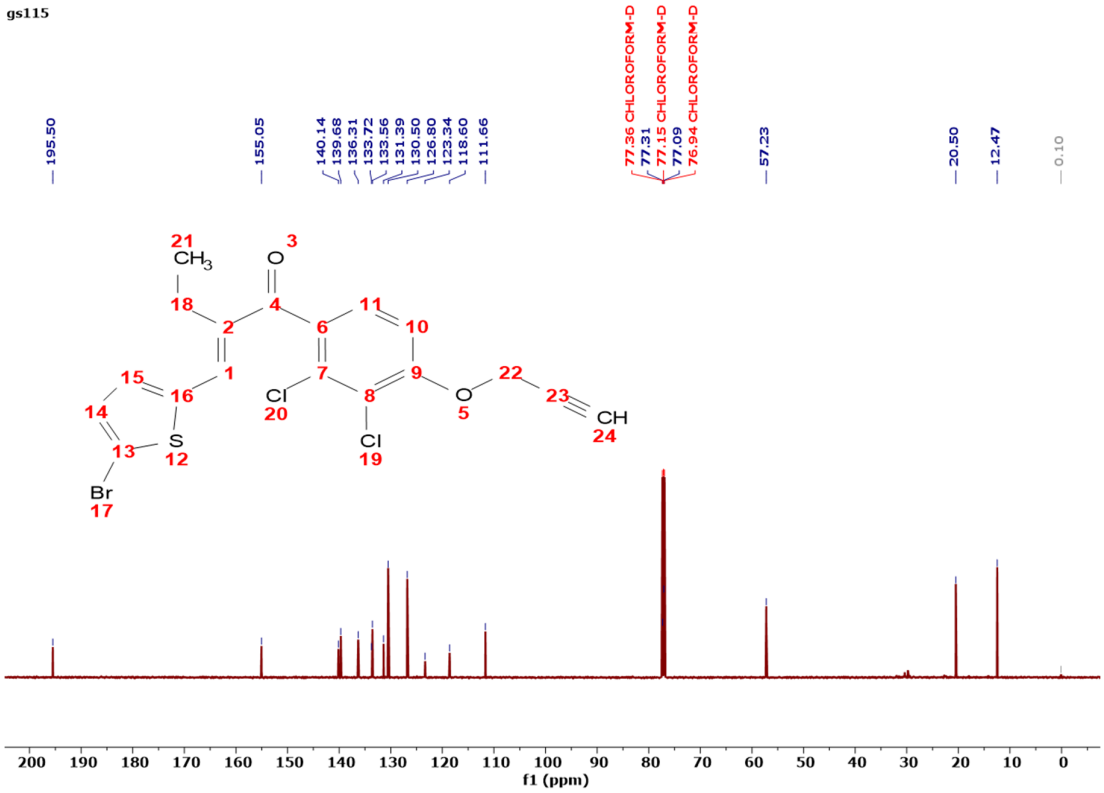


Figure 5. ^{13}C NMR (150.91 MHz, $CDCl_3$) spectrum of compound **8**.

As shown in Figure 6, the ^{1}H NMR spectrum displayed resonances at δ 8.66 (ddd, *J* = 4.8, 1.9, 0.9 Hz, 1H) and 7.69 ppm (td, *J* = 7.7, 1.8 Hz, 1H), corresponding to the pyridine protons H-31 and H-33, respectively. In addition, the singlets at 5.54 and 5.33 ppm, attributed to the OCH_2 and NCH_2 methylene bridges, respectively, also confirm the structure of **11**. The presence of two singlets at 7.59 and 6.96 ppm, corresponding to aromatic protons on the dichlorinated benzene ring, confirms the substitution pattern at positions **7** and **8**. Furthermore, the quartet at 2.95 ppm (*J* = 7.4 Hz, 2H) and triplet at 1.20 ppm (*J* = 7.4 Hz, 3H), attributed to the methylene and methyl groups of the ethyl substituent, respectively, validate the presence of the ethyl group attached to the ketone-bearing aromatic ring.

The ^{13}C NMR spectrum (Figure 7) shows the presence of the carbonyl carbon at 197.0 ppm, confirming the ketone functional group at position 16. The signals at 63.7 and 54.4 ppm correspond to the OCH_2 (C-11) and NCH_2 (C-22) carbons, respectively, while the signals at 19.9 and 13.3 ppm, attributed to the methylene and methyl carbons of the ethyl group, consistent with alkyl substituents on aromatic rings. The aromatic and heteroaromatic carbons appear between 111.6 and 155.8 ppm, with the most downfield signals at 155.8 and 154.6 ppm corresponding to carbons adjacent to nitrogen atoms in the heterocyclic rings, justifying the successful synthesis of the target compound **11**.

2D NMR Spectroscopic Analysis of Compound **8**

For compound **8** (Figure 8), the 2D ^{1}H–^{1}H COSY experiment (Figure 9) confirmed the main proton–proton coupling networks and supported the proposed structural assignment. In particular, the correlation between H-22 and H-24 is consistent with the O–CH_2–C≡CH fragment. Additionally, the NOESY experiment revealed spatial correlations between H-22 and the ring protons H-10 and H-11, providing further structural information and supporting their spatial proximity (Figure 10).

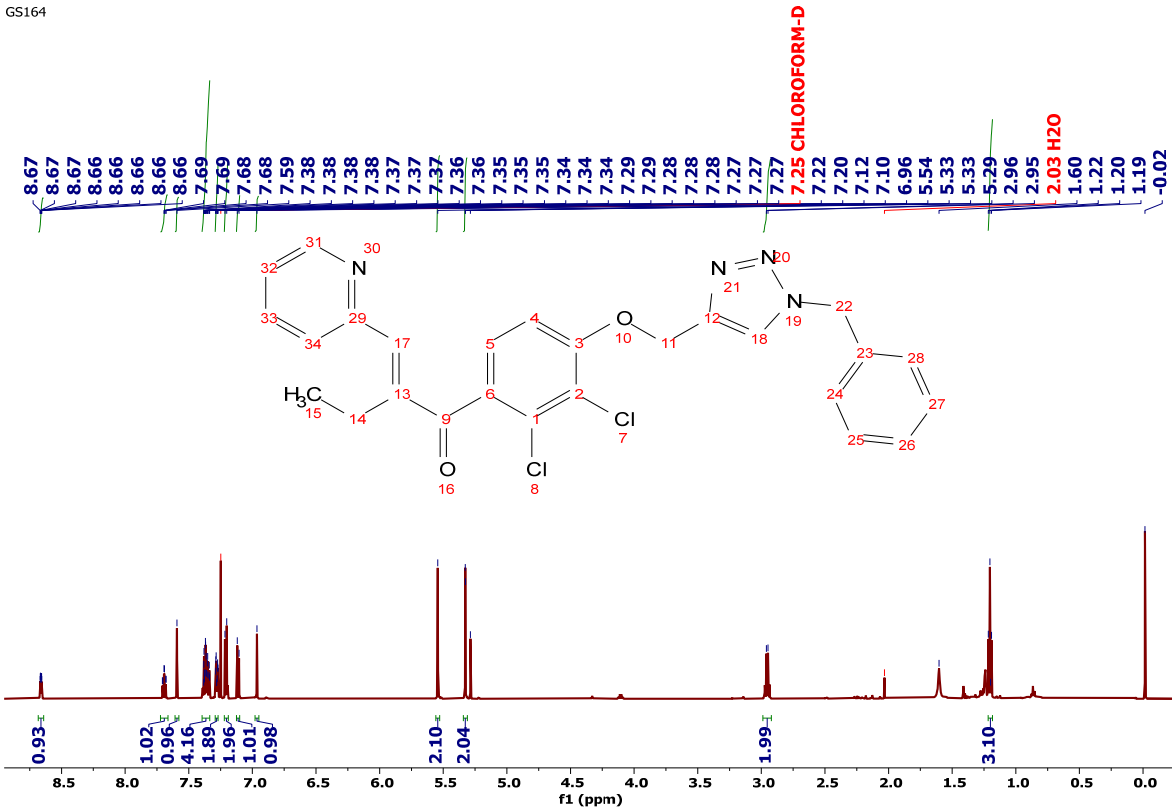


Figure 6. ^{1}H NMR spectrum of compound **11**.

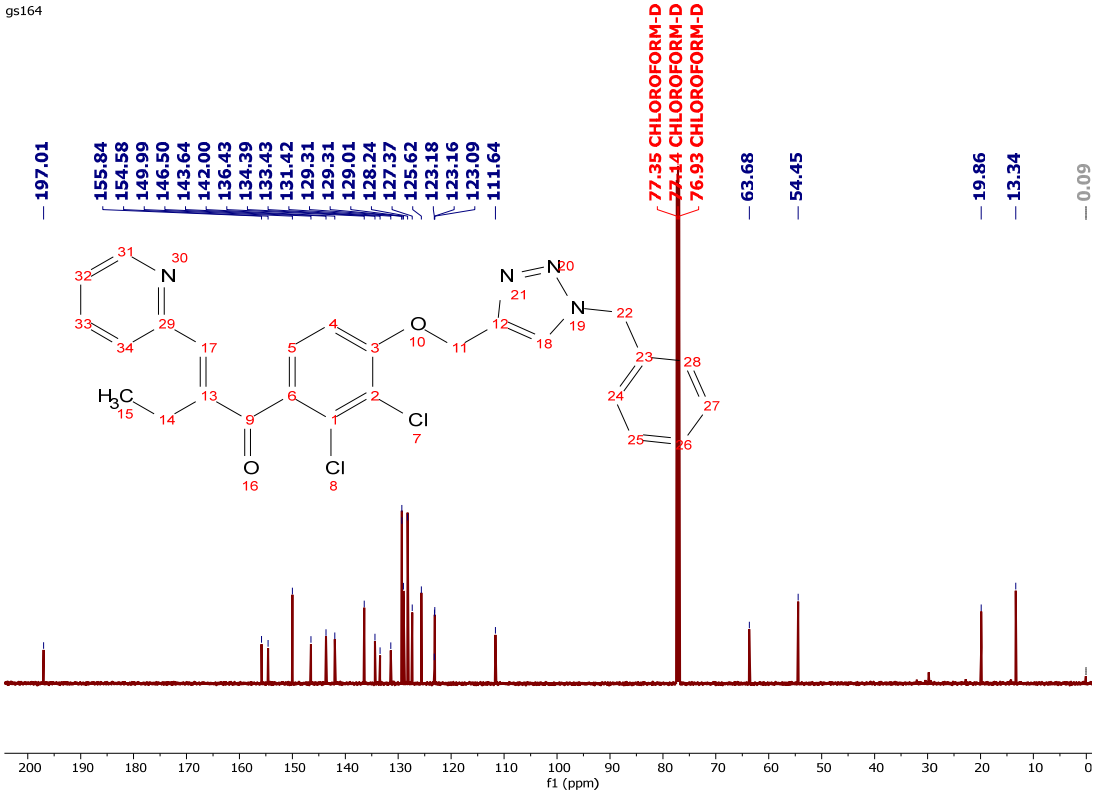


Figure 7. ^{13}C NMR spectrum of compound **11**.

To establish the spatial arrangement of the protons within the molecular framework, a selective NOESY experiment based on the GEMSTONE approach was performed compound **8** (Figure 8). The NOE correlations of interest were located within a highly congested spectral region (6.86–7.18 ppm), where conventional 2D NOESY experiments did not provide sufficient spectral resolution to reliably distinguish the relevant cross-peaks (Figure 10). Increasing the number of points in the direct dimension was insufficient to overcome the severe resonance overlap, while relaxation effects and the intrinsically lower sensitivity of 1D selective experiments further limited the detection of weak NOE correlations.

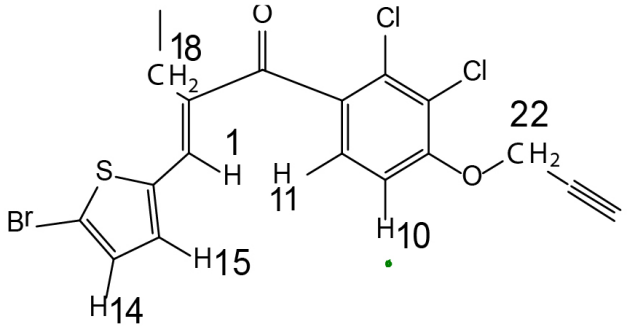


Figure 8. Chemical structure of compound **8**.

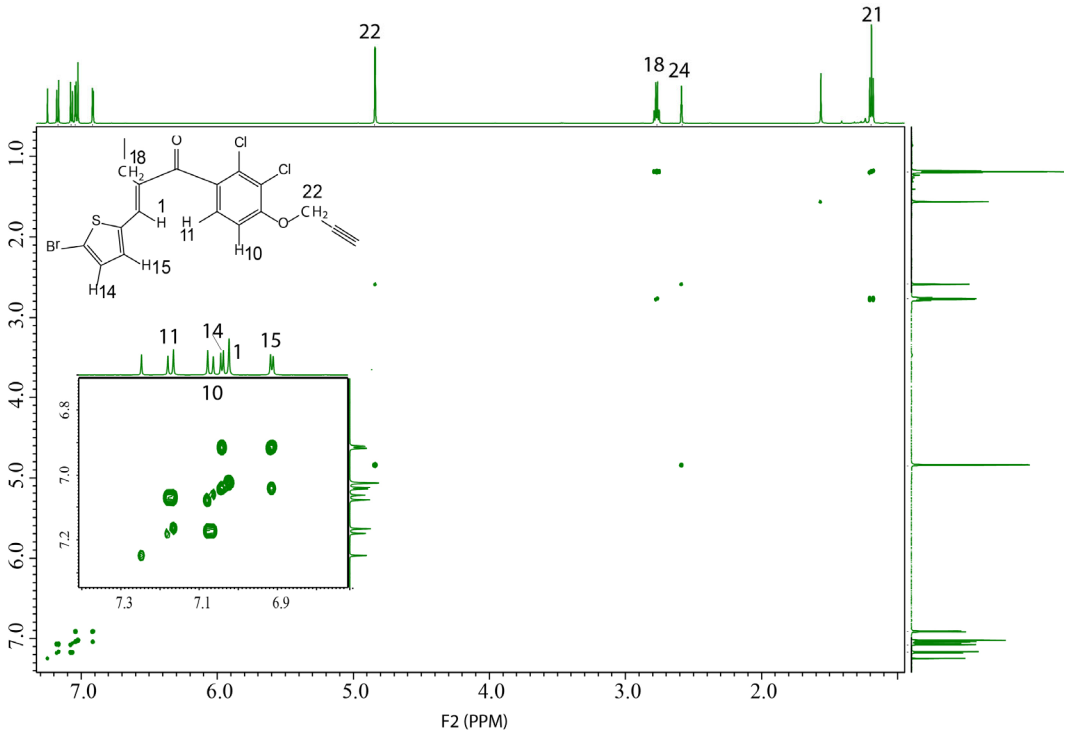


Figure 9. Two-dimensional ^{1}H-^{1}H COSY spectrum of compound **8**.

The GEMSTONE-based selective NOESY experiment was therefore employed to selectively excite individual resonances and probe their spatial proximities within the highly congested spectral region (Figure 11). As an initial experiment, the H1 resonance was selectively excited (orange spectrum). This resonance is separated from the adjacent H11 resonance by only approximately 6 Hz, making their discrimination particularly challeng-

ing using conventional selective excitation approaches. Despite this close frequency separation, the GEMSTONE experiment enabled selective excitation of H1 and revealed clear spatial correlations with H10 and H11, together with a strong correlation with H15. The observed NOE pattern establishes the spatial proximity of H1 to H10, H11, and H15 and provides valuable constraints on their relative spatial arrangement. In particular, the correlation between H1 and H15 supports the proposed spatial orientation of the thienyl-containing moiety, while the H1/H11 correlation provides additional information on the relative positioning of H1 with respect to the adjacent aromatic ring. These complementary spatial correlations are consistent with the proposed molecular structure.

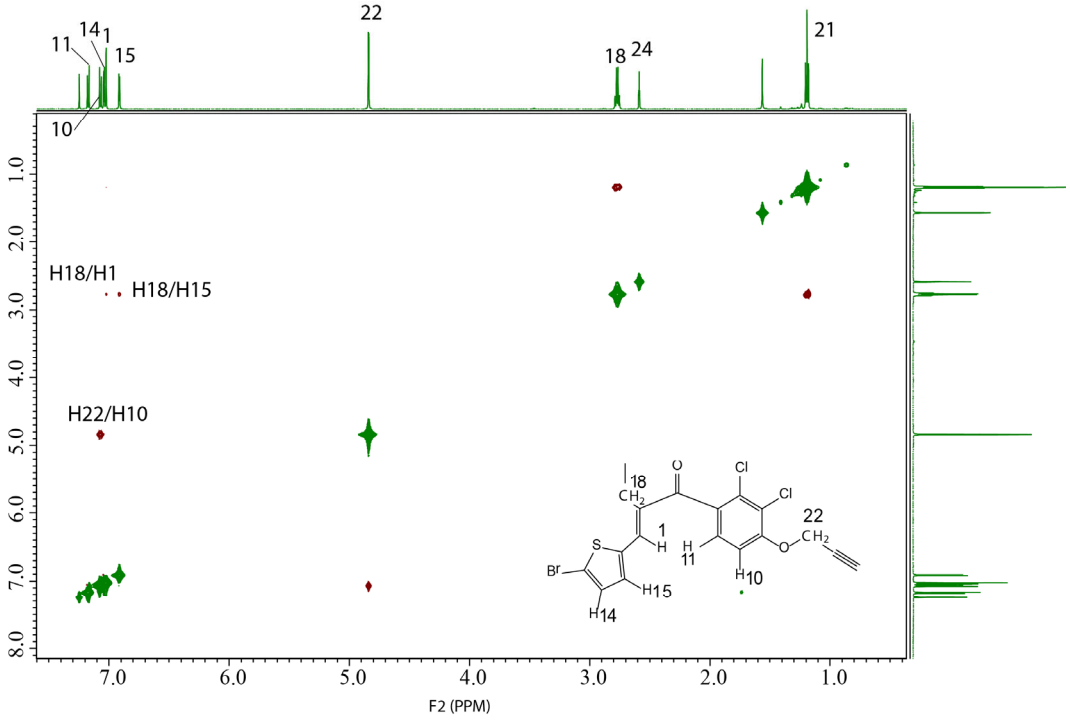


Figure 10. Two-dimensional ^{1}H-^{1}H NOESY spectrum of compound **8**.

A complementary GEMSTONE selective NOESY experiment was subsequently performed by selectively exciting H18 (violet spectrum). This experiment revealed clear NOE correlations between H18 and both H1 and H15, together with a weaker correlation with H11. The observation of an NOE correlation between H18 and H1 indicates that these two protons are in close spatial proximity, as expected for protons located on the two carbons of the C=C double bond. However, the presence of this correlation alone does not allow an unambiguous assignment of the relative configuration of the double bond. In particular, without a reliable reference for the expected NOE intensity or a quantitative analysis of the inter-proton distance, the observed H18/H1 correlation cannot be used to distinguish between a cis- and a trans-arrangement. Therefore, this NOE is considered as evidence of spatial proximity between H18 and H1, but not, by itself, as definitive evidence for either an E or Z configuration.

To further clarify the spatial arrangement, H11 was selectively excited (blue spectrum). In contrast to the H18-selective experiment, selective excitation of H11 revealed an NOE correlation only with H1. The absence of detectable NOE correlations with H15 provides an additional spatial constraint and indicates that H11 occupies a distinct spatial environment relative to these protons. The combination of the H1-, H18-, and H11-selec-

tive NOESY experiments therefore provides a coherent set of spatial constraints that supports the proposed relative configuration of the molecular framework. In particular, the complementary H18/H1 and H11/H1 correlations provide additional evidence for the proposed arrangement around the C=C double bond and help discriminate the proposed structure from alternative relative orientations.

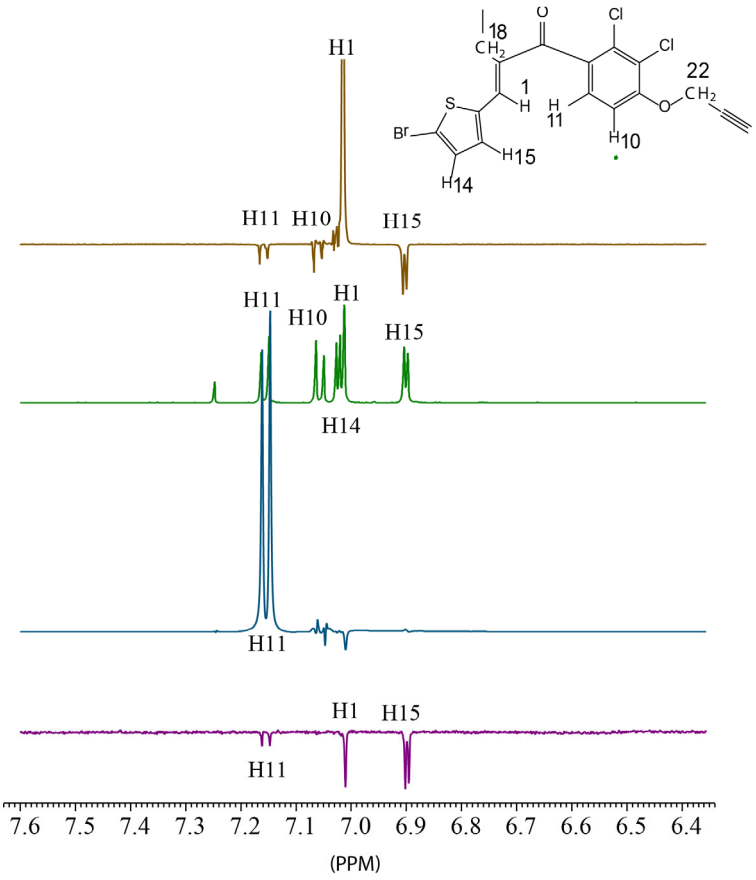


Figure 11. GEMSTONE-selective 1D NOESY spectra of compound **8** showing selective excitation of H1 (orange), H18 (violet), and H11 (blue), with the corresponding NOE correlations.

3.2. Biological Study

3.2.1. Preliminary Single-Dose Cytotoxic Screening

As summarized in Table 1, compounds **4**–**5** and **7**–**10** were subjected to preliminary cytotoxic evaluation against seven human cancer cell lines (HCT116, Caco-2, MDA-MB-231, MDA-MB-468, PC3, Huh7, and MCF7) at a single concentration of 25 µM using an image-based high-content screening assay, with roscovitine tested at 125 µM as the reference compound [32]. Roscovitine was selected as the reference compound because it is a well-established anticancer agent displaying antiproliferative activity against a wide range of human cancer cell lines and is frequently employed as a positive control in cell-based anticancer screening studies. The use of roscovitine in the present work was intended to provide a biologically relevant benchmark for potency comparison rather than a direct structural comparator.

Cell viability was determined relative to DMSO-treated controls. Most derivatives exhibited limited to moderate effects, with cell viabilities ranging from 74 to 94%. Interestingly, the pyridine-substituted derivative **9** reduced cell viability to 54–81% across all tested cell lines, indicating a broader cytotoxic profile comparable to that of roscovitine

despite being evaluated at a five-fold lower concentration. In contrast, the phenyl-substituted analog **10** displayed pronounced effect in MCF7 cells (35% viability) while exerting minimal effects on the remaining cell lines (76–95% viability), suggesting a degree of cell-line selectivity that merits further investigation in dose–response studies.

Table 1. Residual viability (%) ± coefficient of variation (%) following 48 h exposure. Test compounds were evaluated at 25 µM, and roscovitine at 125 µM.

Compound	Cell Lines (Mean % Residual Cells) ± Coefficient of Variation (%)						
	Hct116	**Caco2**	**MDA231**	**MDA468**	**PC3**	**Huh7**	**MCF7**
DMSO	104 ± 6	98 ± 4	101 ± 4	97 ± 5	103 ± 4	100 ± 3	93 ± 10
ROSCO	11 ± 2	14 ± 2	23 ± 2	9 ± 3	25 ± 1	29 ± 3	9 ± 4
4	86 ± 10	84 ± 8	101 ± 8	90 ± 2	91 ± 7	94 ± 4	66 ± 3
5	93 ± 4	91 ± 8	104 ± 6	98 ± 3	99 ± 6	104 ± 6	94 ± 5
7	91 ± 9	89 ± 5	99 ± 5	91 ± 6	95 ± 10	93 ± 10	54 ± 4
8	80 ± 7	83 ± 5	96 ± 4	88 ± 3	91 ± 3	90 ± 8	74 ± 7
9	73 ± 2	58 ± 6	89 ± 4	69 ± 3	81 ± 2	80 ± 4	54 ± 5
10	85 ± 9	76 ± 5	94 ± 9	90 ± 9	95 ± 5	84 ± 4	35 ± 7
11	6 ± 0	17 ± 2	16 ± 3	12 ± 4	24 ± 2	45 ± 4	14 ± 4

Preliminary structure–activity trends could nevertheless be determined from the single-dose screening data. Variations in the chalcone aromatic terminus revealed an apparent influence of electronic effects, following the trend pyridine (**9**) > phenyl (**10**) > bromothiophene (**8**) > furan (**4**,**7**). As illustrated in Figure 12, a heatmap representation provides a visual comparison of cytotoxic profiles of all compound-cell line combinations. It shows the pronounced selectivity of analogs across different cell lines and the more uniform activity pattern exhibited by compound **9**.

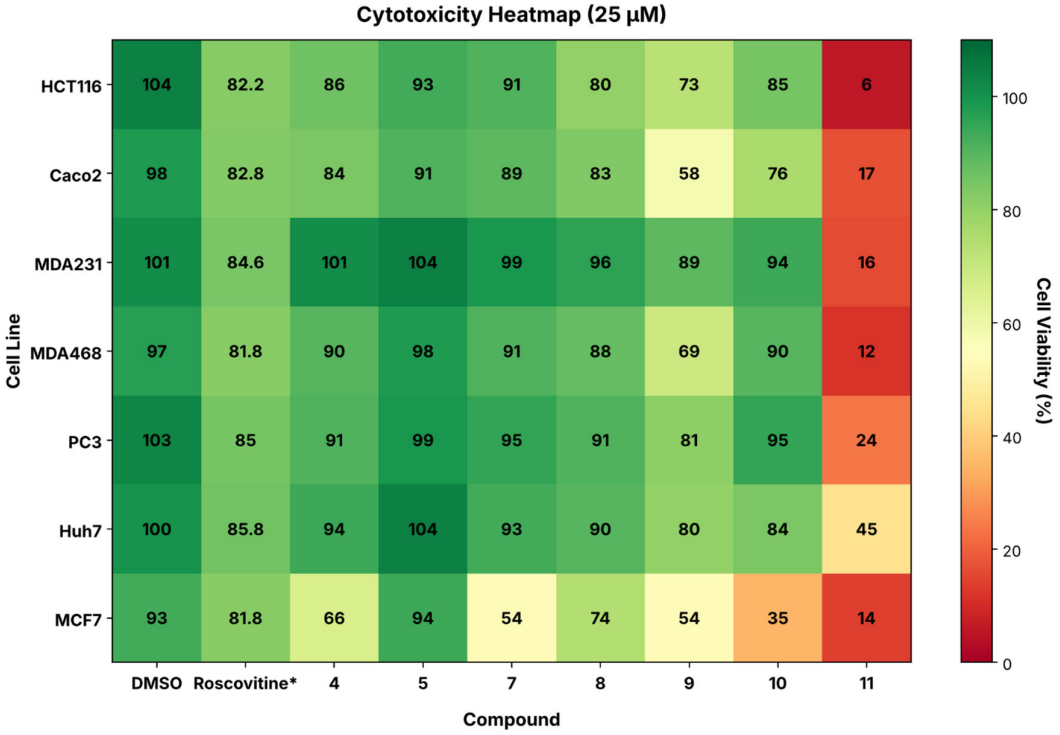


Figure 12. Cytotoxicity heatmap of **4**–**5**, **7**, **8**, **9** and **10** at 25 µM. Color gradient: green (minimal cytotoxicity) to red (high cytotoxicity). Values show percentage cell viability relative to DMSO controls. * Roscovitine values estimated from 125 µM data.

https://doi.org/10.3390/biom16121722

Notably, triazole **11**, obtained from compound **9** via click chemistry, markedly reduced cell viability across all tested cell lines, further supporting these preliminary results. Promising initial screening results, which indicated a degree of cell-line selectivity in certain analogs, prompted us to pursue further dose–response studies.

3.2.2. IC_{50} Determination

Following the preliminary screening, compounds 7, **9**, **10**, and **11** were advanced to full dose–response evaluation across the seven cell-lines (Table 2). Compounds were evaluated over a concentration range of 0.1–25 μM using an image-based high-content screening assay, with roscovitine serving as the reference compound (the test was done in triplicate, and the IC_{50} and amplitude were calculated for each compound).

Compound **11** emerged as the lead, exhibiting IC_{50} values of 6–10 μM across all tested cancer cell lines. In contrast, compounds **7** and **10** showed limited activity (IC_{50} > 25 μM for most cell lines), while compound **9** exhibited moderate, cell-line-dependent activity (IC_{50} = 9–25 μM where active).

Table 2. IC_{50} values (μM) and amplitude (%) of compounds **7**, **9**, **10** and **11** compared with the positive control across various cell lines and fibroblasts after 48 h exposure.

Compound	HuH7 (IC_{50}/A)	HCT116 (IC_{50}/A)	MDA-MB-231 (IC_{50}/A)	MCF7 (IC_{50}/A)	PC3 (IC_{50}/A)	MDA-MB-468 (IC_{50}/A)	Caco2 (IC_{50}/A)	Fibroblasts (IC_{50}/A)
DMSO (%)	NE	NE	NE	NE	NE	NE	NE	NE
ROSCO	17/75	8/93	18/73	7/88	12/78	16/87	14/83	28/55
7	NE/14	NE/16	32/63	NE/22	31/61	NE/12	NE/16	NE/16
9	NE/19	9/35	25/63	NE/58	22/60	22/60	16/60	NE/18
10	NE/60	NE/60	28/60	NE/64	NE/60	NE/62	28/63	NE/65
11	9/65	7.3/98	10/86	6/90	8/84	6/88	6/81	21/69

IC_{50} in μM; NE = No effect; A = amplitude.

Compound **11** demonstrated notable activity against MDA-MB-468 triple-negative breast cancer cells (IC_{50} = 6 μM), representing a 2.7-fold improvement over roscovitine (IC_{50} = 16 μM). This finding is of interest given that triple-negative breast cancers lack targetable hormone receptors and HER2 expression, limiting current therapeutic options beyond cytotoxic chemotherapy. Similar improvements were observed against Caco-2 cells (IC_{50} = 6 μM vs. 14 μM for roscovitine, 2.3-fold) and MCF7 cells (IC_{50} = 6 μM vs. 7 μM, 1.2-fold). Consistent activity was maintained across HuH7 (9 μM), HCT116 (7.3 μM), MDA-MB-231 (10 μM), and PC3 (8 μM), as illustrated in Figure 13A. Comparison with parent compound **9** reveals 2–4-fold potency improvements in cell lines where both compounds were active, suggesting that the triazole modification contributed meaningfully to enhanced cytotoxic activity.

The selectivity profile of compound **11** against normal human dermal fibroblasts (IC_{50} = 21 μM) yielded moderate selectivity indices ranging from 2.1 to 3.5 across the cancer cell panel Figure 13B. with the most favorable windows observed for MCF7, MDA-MB-468, and Caco-2 cells (SI = 3.5 for each). While these values are comparable to roscovitine (fibroblast IC_{50} = 28 μM), it should be noted that roscovitine itself exhibits only modest selectivity and has faced challenges in clinical development due to dose-limiting toxicities and limited efficacy [33]. The moderate selectivity indices of compound **11** indicate that substantial therapeutic window optimization will be necessary before further consideration.

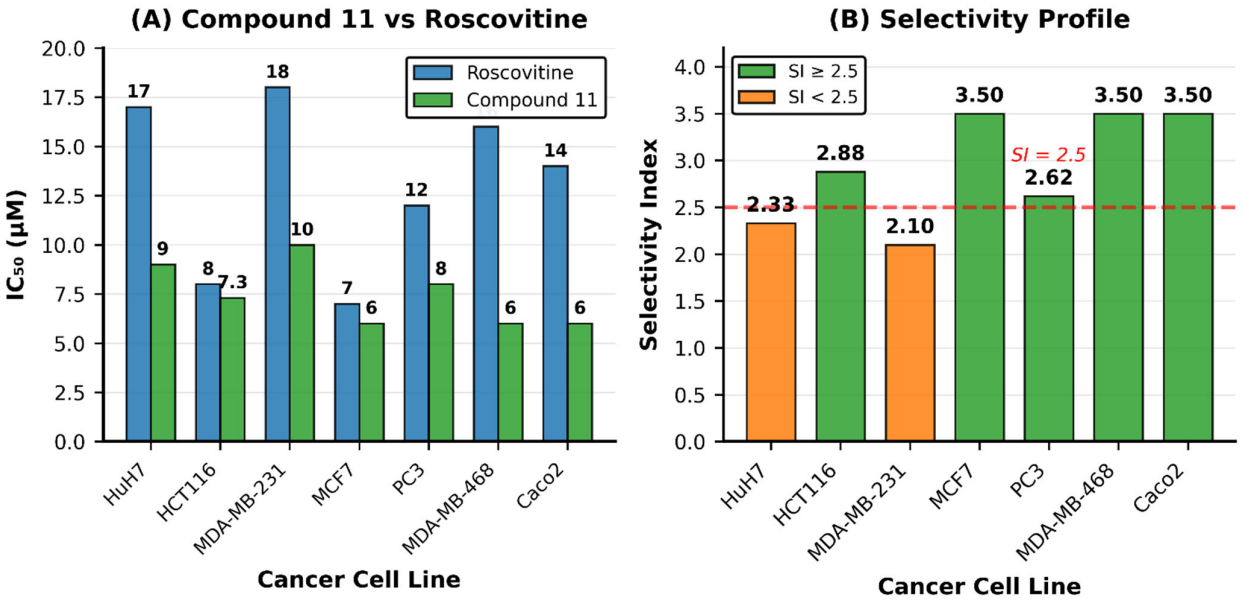


Figure 13. (**A**) IC_{50} comparison of compound **11** with roscovitine. (**B**) Selectivity indices against normal fibroblasts. Green: SI ≥ 2.5; Orange: SI < 2.5; Dashed line: SI threshold.

The contribution of the 1,2,3-triazole moiety to the observed activity likely involves multiple structural factors. The triazole can function as an amide bioisostere [34], potentially establishing hydrogen bonding interactions with target proteins. The triazole nitrogens may serve as H-bond acceptors [35] engaging key residues, while the aromatic heterocycle maintains electronic conjugation and modulates molecular properties [36]. Conformational constraints imposed by the rigid linker could also influence binding geometry [37]. Since roscovitine inhibits CDK1, CDK2, CDK5, and CDK9 [32], compound **11** may exert its activity through CDK inhibition. However, the mechanistic picture is complicated by the **EA** scaffold. **EA** and its derivatives are well-established GST inhibitors [38], and the α,β-unsaturated ketone can act as a Michael acceptor, potentially modifying cysteine residues in multiple proteins [7]. Thus, compound **11** may exert cytotoxicity through CDK inhibition, GST inhibition, dual targeting, or non-specific alkylation. To explore potential molecular targets and rationalize the in vitro potency trends, molecular docking studies were performed against a panel of structurally characterized proteins (Table 3 and Figure 14). Future biochemical validation using recombinant enzyme assays and kinase selectivity profiling will be essential to elucidate the precise mechanism(s) of action.

Table 3. Docking scores of compounds **7**, **9**, **10**, **11** and roscovitine against targets 1HCK, 3DDQ, 4EZ5, 1JDH, 7AAD, 3UG2.

Compound	Docking Score kcal/mol with 7AAD	Docking Score kcal/mol with 4EZ5	Docking Score kcal/mol with 3UG2	Docking Score kcal/mol with 3DDQ	Docking Score kcal/mol with 1HCK	Docking Score kcal/mol with 1JDH
7	−13.648	−10.940	−9.673	−12.542	−11.210	−8.545
9	−12.916	−12.267	−9.707	−15.402	−12.422	−9.455
10	−13.993	−11.617	−10.870	−11.817	−12.033	−10.001
11	−20.365	−14.266	−14.467	−15.532	−16.706	−11.916
Cocrystallized ligand	−17.819	−15.740	−14.076	−14.344	−41.844	NA
Roscovitine	−14.462	−14.060	−9.747	−14.436	−13.068	−9.264

Redocked ligand RMSD (Å)	1.40	1.71	2.15	1.07	1.57	NA

Co-crystallized ligands were redocked; pose reproduction accuracy was confirmed by RMSD (<2.0 Å) between crystallographic and redocked poses.

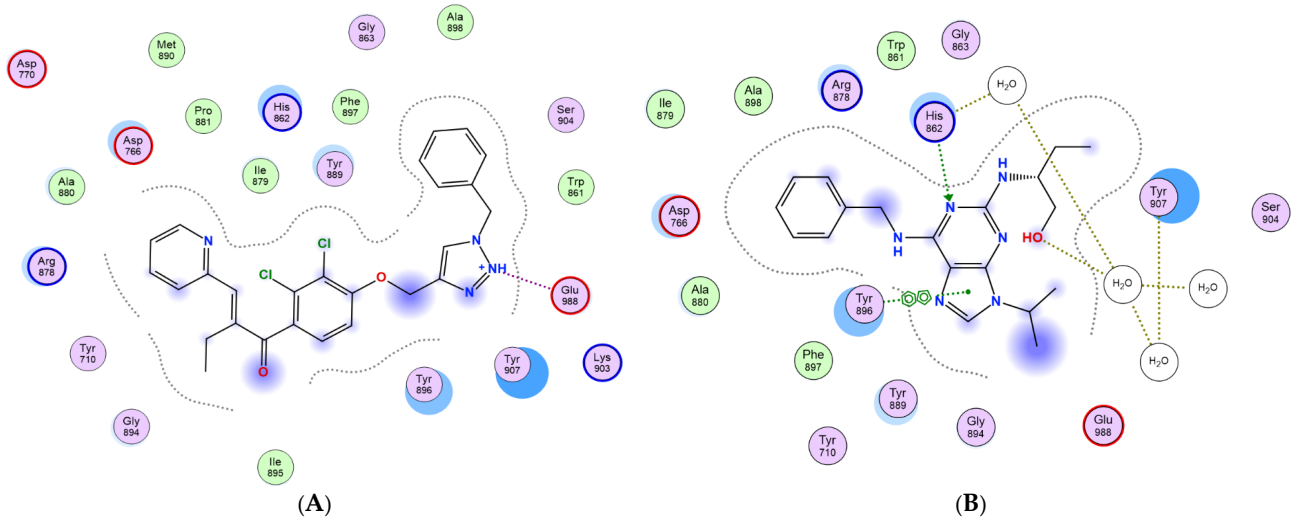


Figure 14. (**A**) Compound **11** (**left**) vs. (**B**) Roscovitine (**right**) docked with 7AAD.

3.3. Results of Molecular Docking

Since the precise molecular target responsible for the antiproliferative activity of the synthesized **EA**-based chalcone derivatives remains unknown, a multi-target docking strategy was employed as a hypothesis-generating approach. The selected protein structures represent cancer-relevant targets involved in cell proliferation, cell-cycle progression, signal transduction, apoptosis, and tumor development. These targets were chosen based on their established roles in oncogenic pathways, the availability of high-resolution crystallographic structures, and previous reports demonstrating their suitability for anticancer ligand screening. Consequently, the docking study was intended to identify potential molecular interactions capable of contributing to the observed biological activity rather than to establish a definitive mechanism of action.

Targets were selected to represent cancer-relevant signaling enzymes and clinically actionable pathways, while enabling benchmarking against the reference inhibitor roscovitine. Accordingly, to explore potential molecular targets and rationalize the in vitro potency trends, compounds **7**, **9**, **10** and **11** were docked against six protein structures (PDB IDs: 1HCK, 3DDQ, 4EZ5, 1JDH, 7AAD and 3UG2) using a consistent docking workflow. Roscovitine was included as a reference ligand where applicable. The docking scores for all ligand–target combinations are summarized in Table 3, and representative interaction diagrams for compound **11** versus roscovitine are shown in Figure 14.

To validate the docking workflow, the co-crystallized ligand for each structure (except for 1JDH) was extracted and re-docked into the corresponding binding pocket. The re-docked poses reproduced the experimental binding modes with RMSD values of 1.07–2.15 Å (Table 3), supporting the reliability of the docking protocol.

Overall, the docking results were aligned with the biological ranking (Table 2): the lead triazole **11** generally achieved more favorable scores and/or more extensive interaction networks than the parent alkyne **9** and the less active analogs **7** and **10**. This supports the interpretation that CuAAC-derived triazole installation is not only a synthetic extension, but also a functional pharmacophore that can strengthen polar binding interactions while retaining hydrophobic complementarity within druggable pockets.

In PARP1 (PDB: 7AAD), the 2D interaction maps (Figure 14A,B) highlight clear differences in how compound **11** and roscovitine are accommodated within the binding pocket. Compound **11** (Figure 14A) is positioned deep in the cavity and is stabilized by a clear direct hydrogen-bond interaction with Glu988 (via the triazole/adjacent polar region), while its aromatic/halogenated scaffold occupies a predominantly hydrophobic environment and shows extensive complementarity with residues in the Tyr/Phe/His-rich region (e.g., Tyr896, Tyr907, Phe897, His862, and nearby aliphatic residues). In contrast, roscovitine (Figure 14B) displays a more polar interaction pattern dominated by a water-mediated hydrogen-bond network around the hydroxyl group, with additional contacts in the Tyr/His region (notably Tyr907 and His862). Collectively, these features support the stronger docking score of **11** in 7AAD, as it combines a direct anchoring interaction with effective pocket filling, whereas roscovitine relies more heavily on bridging waters to maintain polar contacts.

Across the remaining targets, compound **11** repeatedly leveraged the triazole and ether linkers as hydrogen-bond acceptors or donors while the chalcone-**EA** scaffold filled hydrophobic regions, whereas the less active analogs (**7**, **9** and **10**) typically presented fewer strong polar anchors and/or less optimal shape complementarity (Table 3). Collectively, these docking trends are compatible with the IC_{50} profile of 11 (6–10 μM across all cancer cell lines) and with its 2–4-fold improvement over compound **9** in the cell lines where both compounds were active (Table 2).

Importantly, docking to PDB 1JDH was performed using a manually defined pocket because no co-crystallized ligand was available to guide binding-site selection. Consequently, the 1JDH poses and scores should be interpreted as hypothesis-generating rather than definitive, and they should be validated using complementary pocket prediction, alignment to ligand-bound homologous structures, or experimental data. Taken together, the docking outcomes support the role of the triazole linker in **11** as a key contributor to stabilizing productive binding poses across multiple targets, and they motivate follow-up biochemical assays to confirm target engagement.

3.4. In-Silico ADME, Drug-likeness and Toxicity Prediction

In-silico ADME and toxicity predictions were performed for compounds **7**, **9**, **10**, and **11** to support lead prioritization. All compounds were predicted to have high gastrointestinal absorption, and all complied with Veber rules, indicating acceptable polarity/flexibility profiles for oral drug-likeness. According to Lipinski screening, compounds **7**, **9**, and **11** showed zero violations, whereas compound **10** presented one violation (MLOGP > 4.15), suggesting comparatively higher lipophilicity. Solubility predictions (ESOL LogS) indicated that compounds **7** and **9** had similar values (−5.08 and −5.07), compound **10** was slightly less soluble (−5.72), and compound **11** showed the lowest predicted solubility (−6.32). Although reduced solubility may negatively impact formulation or exposure, compound **11** remains within a range frequently encountered for hydrophobic anticancer scaffolds, and this parameter can be addressed through salt selection, co-solvents, or nanoformulation strategies if required. Regarding distribution-related parameters, compounds **7**, **9**, and **10** were predicted to be BBB permeable, while compound **11** was predicted as non-BBB permeable, which may be advantageous by potentially reducing CNS-related adverse effects for a non-CNS oncology indication. SwissADME predictions suggested possible drug–drug interaction risk for some analogs, with CYP1A2 inhibition predicted for **7**, **9** and **10**, while CYP3A4 inhibition was predicted for **9**, **10** and the lead compound **11** (Table 4). These in-silico findings highlight CYP profiling as a recommended follow-up during lead optimization.

Toxicity predictions supported the overall developability of the series. Carcinogenicity and mutagenicity were predicted inactive for all compounds, and hepatotoxicity probabilities were modest; notably, compound **7** showed the highest hepatotoxicity probability label among the series. Acute toxicity (LD_{50}) values suggested that compounds **7**, **9**, and **10** fall in a similar range (≈1500–1632 mg/kg), while compound **11** displayed a lower LD_{50} (600 mg/kg), indicating comparatively higher acute toxicity potential.

Taken together, these results indicate that compound **11** remains the lead candidate from an efficacy standpoint, but its lower predicted solubility and lower LD_{50} highlight that future optimization should prioritize improving physicochemical properties and therapeutic index while maintaining the favorable activity and docking profile.

Table 4. Predicted ADME parameters, drug-likeness rules, and toxicity endpoints for compounds **7**, **9**, **10**, and **11** (SwissADME, ADMETlab/ADMETmesh, and ProTox-II).

	ADME							Drug Likeness		Toxicity			
Code	**Water Solubility Log S (ESOL)**	**GI Absorption**	**BBB Permeability**	**CYP 1A2 Inhibitor**	**CYP3A4 Inhibitor**	**VD (L/kg)**	**Total CL (mL/min/kg)**	**Lipinski**	**Veber**	**Hepatotoxicity (Probability)**	**Carcinogenicity**	**Mutagenicity**	**LD50 Value (mg/kg)**
7	−5.08	High	Yes	Yes	No	1.997	6.781	Yes; 0 violation	Yes	0.56 (Active)	0.55 (Inactive)	0.54 (Inactive)	1500
9	−5.07	High	Yes	Yes	Yes	0.939	3.309	Yes; 0 violation	Yes	0.56 (Inactive)	0.62 (Inactive)	0.67 (Inactive)	1632
10	−5.72	High	Yes	Yes	Yes	0.791	5.170	Yes; 1 violation: MLOGP > 4.15	Yes	0.57 (Inactive)	0.62 (Inactive)	0.66 (Inactive)	1632
11	−6.32	High	No	No	Yes	0.763	8.388	Yes; 0 violation	Yes	0.55 (Inactive)	0.63 (Inactive)	0.54 (Inactive)	600

3.5. DFT Study

DFT calculations were performed at the B3LYP/6-311G level for the neutral singlet ground state in the gas phase. The geometries of compounds **8** and **11** were fully optimized, and frequency calculations confirmed that the resulting structures are true minima (no imaginary frequencies). These optimized structures were used to compute the total electronic energy, dipole moment, polarizability, thermodynamic parameters, and frontier molecular orbital (HOMO-LUMO) energies.

Compound **8** exhibits a dipole moment of 3.69 Debye, indicating moderate polarity, and a polarizability of 265 a.u., reflecting electronic flexibility. Thermodynamic parameters, including a thermal energy of 171.93 kcal/mol, heat capacity, and entropy values, suggests a stable conjugated framework with balanced rigidity and adaptability (Table 5). Compound **11** exhibits a dipole moment of 7.25 Debye, indicating a markedly higher polarity than compound **8**, and a polarizability of 317 a.u., reflecting a more easily distorted electron cloud. Its thermodynamic parameters, including a thermal energy of 292.44 kcal/mol, a heat capacity of 112.58 cal/mol·K and an entropy of 203.85 cal/mol·K (Table 5). The frontier orbital energies give a HOMO-LUMO gap of 4.29 eV, considerably smaller than that of compound **8** (6.60 eV), which points to higher chemical reactivity and polarizability for compound **11**.

Such characteristics may facilitate molecular recognition and ligand-protein interactions, potentially contributing to the improved antiproliferative activity observed experimentally. Although DFT calculations alone cannot directly predict biological activity, they

provide complementary insight into the electronic features that distinguish the lead compound from less active analogs.

Table 5. Calculated thermodynamic and electronic parameters of compound **8** and **11** at the B3LYP/6-311G level.

Compound	E_{total} (eV)	Dipole Moment (μ)	Polarizability (α)	E (Thermal)	Heat Capacity (Cv)	Entropy (S)	E_{HOMO} (eV)	E_{LUMO} (eV)
8	−4733.196	3.686 Debye	265.350 a.u	171.930 kcal/mol	85.792 cal/mol.K	180.490 cal/mol.K	−7.374	−0.776
11	−2293.363	7.253 Debye	317.316 a.u	292.438 kcal/mol	112.581 cal/mol.K	203.852 cal/mol.K	−6.504	−2.210

3.5.1. Molecular Geometry Optimization

The optimized geometry of compound **8** and **11** were obtained at the B3LYP/6-311G level of theory (Figures 15 and 16). The structure of **8** adopts a predominantly planar conformation across the aromatic and conjugated framework, which facilitates effective π-electron delocalization. The substituents are oriented to minimize steric repulsion, resulting in an extended geometry consistent with a trans (E) configuration (Figure 15a). This planarity enhances electronic communication throughout the framework and contributes to stabilization of the conjugated system. The corresponding molecular electrostatic potential (MESP) plot further illustrates the electronic distribution across the optimized geometry, highlighting regions of electron density and potential reactivity (Figure 15b).

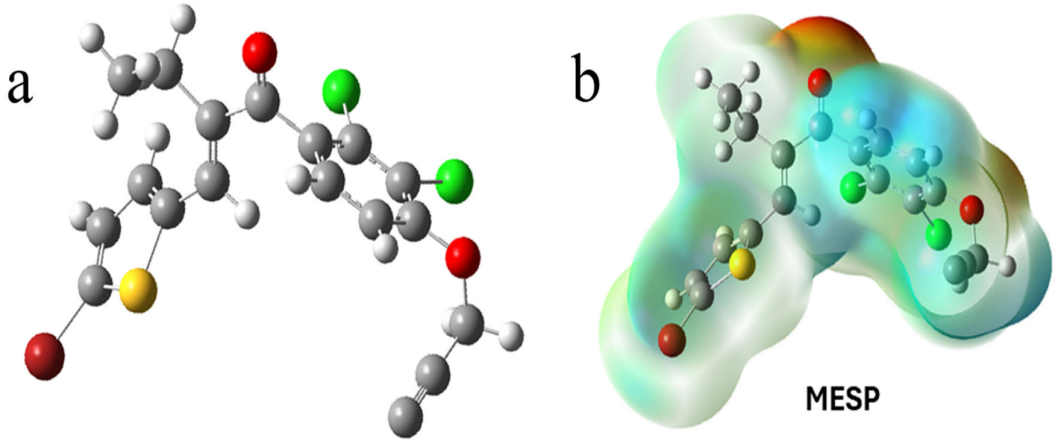


Figure 15. (**a**) Optimized structure of compound **8**; (**b**) MESP plot of compound **8**.

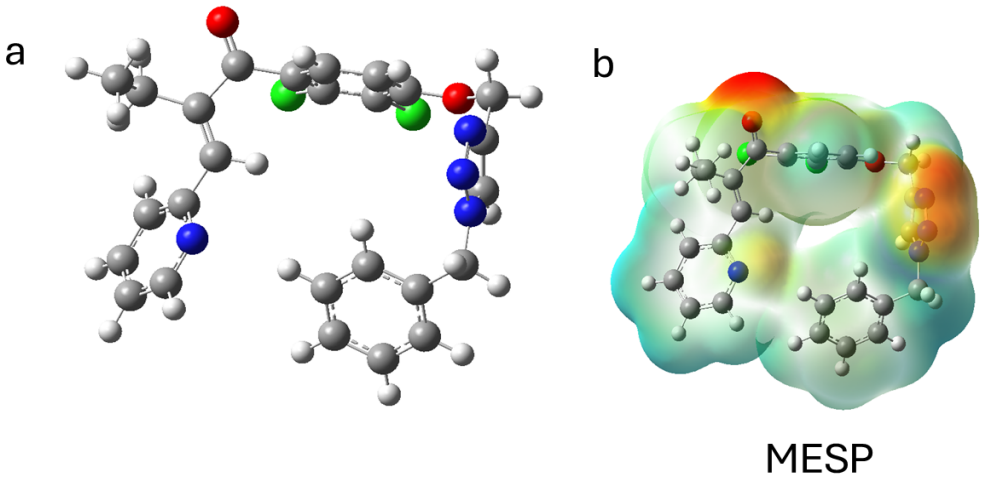


Figure 16. (**a**) Optimized structure of compound **11**; (**b**) MESP plot of compound **11**.

3.5.2. Frontier Molecular Orbital (HOMO–LUMO) Analysis

Frontier molecular orbital analysis provides insight into the electronic distribution and reactivity of compound **8**. The HOMO is primarily localized over the aromatic and conjugated regions, indicating electron-rich domains, whereas the LUMO is distributed over electron-deficient regions of the molecule. The calculated energies of the HOMO and LUMO are −7.374 eV and −0.776 eV, respectively, giving an energy gap of approximately 6.504 eV (Figure 17). This relatively large gap suggests that **8** possesses significant electronic stability and limited low-energy excitations. excitations compared to compound **8**.

In contrast, the click triazole product **11** exhibits a noticeably compressed energy gap of 4.294 eV (with a HOMO of -6.504 eV and a LUMO of −2.210 eV) compared to the terminal alkyne derivative **8**, indicating that the formation of the heterocycle extends the conjugated framework, leading to increased reactivity and a greater propensity for lower-energy electronic excitations (Figure 17).

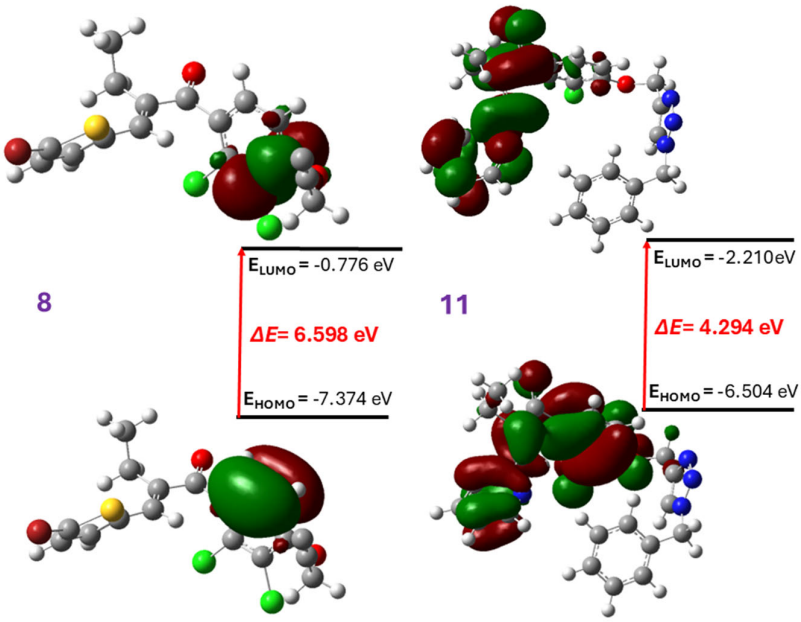


Figure 17. Frontier molecular orbitals (HOMO-LUMO) of compounds **8** and **11**.

4. Conclusions

In this study, we report seven novel EA-based chalcone derivatives bearing click-compatible propargyl/allyl handles. SAR studies across seven cancer cell lines revealed electronic modulation trends (pyridine > phenyl > bromothiophene > furan) and propargyl ether superiority. CuAAC-mediated conversion of lead **9** to triazole **11** yielded IC_{50} 6–10 μM across cancer lines, with 2.7-fold improvement over roscovitine in triple-negative breast cancer cells (MDA-MB-468) and acceptable selectivity (SI = 2.1–3.5). In parallel, molecular docking against a panel of targets (PDB IDs: 1HCK, 3DDQ, 4EZ5, 3UG2, 7AAD, and 1JDH) consistently ranked compound **11** as the top-scoring ligand relative to the parent analogs and roscovitine, with the strongest predicted advantage observed for PARP1 (7AAD) and 3UG2. Binding-mode analysis in PARP1 (7AAD) further supported this trend, showing a direct anchoring interaction for compound **11** (notably with Glu988) and extensive hydrophobic complementarity, whereas roscovitine relied more heavily on water-mediated polar contacts. In-silico ADMET/toxicity predictions indicated high gastrointestinal absorption and overall drug-likeness for the series; however, compound **11** showed comparatively lower predicted solubility and a lower LD_{50}, highlighting physicochemical optimization as a priority during lead progression. The combined NMR and DFT analyses support the proposed E-configuration and electronic structure of compound **8.** The HOMO-LUMO distribution, moderate energy gap, and relatively high polarizability reflect efficient π-electron delocalization and enhanced electronic responsiveness, offering insight into the molecular electronic properties and reactivity.

Collectively, this work represents the first integration of chalcone-type Michael acceptors with click-compatible handles into the EA scaffold, demonstrating that triazole formation enhances anticancer potency while preserving selectivity comparable to the reference compound, roscovitine. Future directions include GST isoform profiling, click-mediated probe synthesis for target identification, and in vivo efficacy assessment of compound **11** in xenograft models, alongside formulation/medicinal-chemistry optimization to improve solubility and safety margins.

Supplementary Materials: The following supporting information can be downloaded at: https://www.mdpi.com/article/10.3390/biom16121722/s1, File S1: Figure S1. ^{1}H NMR Spectrum of compound **4** in $CDCl_3$; Figure S2. ^{13}C NMR Spectrum of compound **4** in $CDCl_3$; Figure S3. ^{1}H NMR Spectrum of compound **5** in $CDCl_3$; Figure S4. ^{13}C NMR Spectrum of compound **5** in $CDCl_3$; Figure S5. ^{1}H NMR Spectrum of compound **7** in $CDCl_3$; Figure S6. ^{13}C NMR Spectrum of compound **7** in $CDCl_3$; Figure S7. ^{1}H NMR Spectrum of compound **9** in $CDCl_3$; Figure S8. ^{13}C NMR Spectrum of compound **9** in $CDCl_3$; Figure S9. ^{1}H NMR Spectrum of compound **10** in $CDCl_3$; Figure S10. ^{13}C NMR Spectrum of compound **10** in $CDCl_3$; Figure S11.^{1}H NMR Spectrum of compound **8** in CDC_{13}; Figure S12.^{13}C NMR Spectrum of compound **8** in CDC_{13}; Figure S13.^{1}H NMR Spectrum of compound **11** in CDC_{13}; Figure S14.^{13}C NMR Spectrum of compound **11** in CDC_{13}.

Author Contributions: Conceptualization, G.S., H.H. and S.E.K.; methodology, G.S. and H.H.; formal analysis, G.S., H.H., H. D., N.E.B. and S.E.K.; investigation, G.H., N.E.B., G.G. and S.E.K.; validation, H. D., N.E.B., G.G. and S.E.K.; resources, G.H., G.G. and S.E.K.; data curation, G.H., G.S. and H.H.; writing—original draft preparation, G.S., H.H. and H.D.; writing—review and editing, G.H., H. D., N.E.B., G.G. and S.E.K.; visualization, G.S., H.H., H.D., N.E.B. and S.E.K.; supervision, N.E.B., G.G. and S.E.K. All authors have read and agreed to the published version of the manuscript.

Funding: This research received no external funding.

Institutional Review Board Statement: Not applicable.

Informed Consent Statement: Not applicable.

Data Availability Statement: Data supporting the findings of this study are available within the manuscript and its supplementary materials.

Acknowledgments: The authors gratefully acknowledge the support of Euromed University of Fes (UEMF), Morocco, and the African Scientific, Research and Innovation Council (ASRIC).

Conflicts of Interest: The authors declare no conflicts of interest.

Abbreviations

EA = ethacrynic acid, MDR = multidrug resistance, GSTs = glutathione S-transferases, CuAAC = Cu(I)-catalyzed azide-alkyne cycloaddition, SAR = nstructure-activity relationship, TLC = thin-layer chromatography, DFT = density functional theory.

References

1. Sung, H.; Ferlay, J.; Siegel, R.L.; Laversanne, M.; Soerjomataram, I.; Jemal, A.; Bray, F. Global cancer statistics 2020: GLOBOCAN estimates of incidence and mortality worldwide for 36 cancers in 185 countries. *CA Cancer J. Clin.* **2021**, *71*, 209–249. https://doi.org/10.3322/caac.21660.
2. Dunn, J. It is time to close the gap in cancer care. *JCO Glob. Oncol.* **2023**, *9*, e2200429. https://doi.org/10.1200/GO.22.00429.
3. Li, L.; Shan, T.; Zhang, D.; Ma, F. Nowcasting and forecasting global aging and cancer burden: Analysis of data from the GLOBOCAN and Global Burden of Disease Study. *J. Natl. Cancer Cent.* **2024**, *4*, 223–232. https://doi.org/10.1016/j.jncc.2024.05.002.
4. Dhiman, V.K.; Kumari, M.; Singh, D. Chemoresistance: The hidden barrier in cancer treatment. *Cancer Pathog. Ther.* **2026**, *4*, 98–109. https://doi.org/10.1016/j.cpt.2025.07.001.
5. Abouzeid, H.A.; Liu, X.; Abuelhana, A. Emerging strategies to overcome chemotherapy resistance in breast cancer. *Discov. Med.* **2025**, *2*, 290. https://doi.org/10.1007/s44337-025-00470-y.
6. Alnasser, S.M. The role of glutathione S-transferases in human disease pathogenesis and their current inhibitors. *Genes Dis.* **2025**, *12*, 101482. https://doi.org/10.1016/j.gendis.2024.101482.
7. Townsend, D.M.; Tew, K.D. The role of glutathione-S-transferase in anti-cancer drug resistance. *Oncogene* **2003**, *22*, 7369–7375. https://doi.org/10.1038/sj.onc.1206940.
8. Chatterjee, A.; Gupta, S. The multifaceted role of Glutathione S-transferases in cancer. *Cancer Lett.* **2018**, *433*, 33–42. https://doi.org/10.1016/j.canlet.2018.06.028.
9. Lei, Z.-N.; Tian, Q.; Teng, Q.-X.; Wurpel, J.N.D.; Zeng, L.; Pan, Y.; Chen, Z.-S. Understanding and targeting resistance mechanisms in cancer. *MedComm* **2023**, *4*, e265. https://doi.org/10.1002/mco2.265.
10. Yu, L.; Lee, H.; Rho, S.B.; Park, M.K.; Lee, C.H. Ethacrynic acid: A promising candidate for drug repurposing as an anticancer agent. *Int. J. Mol. Sci.* **2023**, *24*, 6712. https://doi.org/10.3390/ijms24076712.
11. El Brahmi, N.; El Abbouchi, A.; El Kazzouli, S. An overview on the synthesis and anticancer properties of ethacrynic acid and their analogues. *Results Chem.* **2023**, *6*, 101117. https://doi.org/10.1016/j.rechem.2023.101117.
12. El Abbouchi, A.; El Brahmi, N.; Hiebel, M.-A.; Bignon, J.; Guillaumet, G.; Suzenet, F.; El Kazzouli, S. Synthesis and evaluation of a novel class of ethacrynic acid derivatives containing triazoles as potent anticancer agents. *Bioorg. Chem.* **2021**, *115*, 105293. https://doi.org/10.1016/j.bioorg.2021.105293.
13. Mignani, S.; El Brahmi, N.; El Kazzouli, S.; Eloy, L.; Courilleau, D.; Caron, J.; Bousmina, M.M.; Caminade, A.-M.; Cresteil, T.; Majoral, J.-P. A novel class of ethacrynic acid derivatives as promising drug-like potent generation of anticancer agents with established mechanism of action. *Eur. J. Med. Chem.* **2016**, *122*, 656–673. https://doi.org/10.1016/j.ejmech.2016.05.063.
14. Punganuru, S.R.; Mostofa, A.G.M.; Madala, H.R.; Basak, D.; Srivenugopal, K.S. Potent anti-proliferative actions of a non-diuretic glucosamine derivative of ethacrynic acid. *Bioorg. Med. Chem. Lett.* **2016**, *26*, 2829–2833. https://doi.org/10.1016/j.bmcl.2016.04.062.
15. El Abbouchi, A.; El Brahmi, N.; Hiebel, M.-A.; Ghammaz, H.; El Fahime, E.; Bignon, J.; Guillaumet, G.; Suzenet, F.; El Kazzouli, S. Improvement of the chemical reactivity of michael acceptor of ethacrynic acid correlates with antiproliferative activities. *Molecules* **2023**, *28*, 910. https://doi.org/10.3390/molecules28020910.
16. El Abbouchi, A.; Mkhayar, K.; Elkhattabi, S.; El Brahmi, N.; Hiebel, M.-A.; Bignon, J.; Guillaumet, G.; Suzenet, F.; El Kazzouli, S. Design, synthesis, computational studies, and anti-proliferative evaluation of novel ethacrynic acid derivatives containing nitrogen heterocycle, urea, and thiourea moieties as anticancer agents. *Molecules* **2024**, *29*, 1437. https://doi.org/10.3390/molecules29071437.

17. Yang, X.; Liu, G.; Li, H.; Zhang, Y.; Song, D.; Li, C.; Wang, R.; Liu, B.; Liang, W.; Jing, Y.; et al. Novel oxadiazole analogues derived from ethacrynic acid: Design, synthesis, and structure−activity relationships in inhibiting the activity of glutathione s-transferase P1-1 and cancer cell proliferation. *J. Med. Chem.* **2010**, *53*, 1015–1022. https://doi.org/10.1021/jm9011565.
18. Dong, J.; Yang, D.; Zhao, G. Encouraging effects of ethacrynic acid derivatives possessing a privileged α,β-unsaturated carbonyl structure scaffold. *Med. Chem.* **2018**, *8*, 185–191. https://doi.org/10.4172/2161-0444.1000511.
19. El Abbouchi, A.; El Brahmi, N.; Hiebel, M.-A.; Bignon, J.; Guillaumet, G.; Suzenet, F.; El Kazzouli, S. Synthesis and biological evaluation of ethacrynic acid derivatives bearing sulfonamides as potent anti-cancer agents. *Bioorg. Med. Chem. Lett.* **2020**, *30*, 127426. https://doi.org/10.1016/j.bmcl.2020.127426.
20. Saghdani, N.; El Abbouchi, A.; El Brahmi, N.; Idir, A.; Otmane Rachedi, K.; Berredjem, M.; Haloui, R.; Elkhattabi, S.; Ait Mouse, H.; Ben Hadda, T.; et al. Design, synthesis, in-vitro, in-silico, DFT and POM studies of a novel family of sulfonamides as potent anti-triple-negative breast cancer agents. *Comput. Biol. Chem.* **2024**, *113*, 108214. https://doi.org/10.1016/j.compbiolchem.2024.108214.
21. Yildirim, M.; Suleiman, G. A practical access to new pyrrolizine carboxylates via KHMDS-catalyzed carbocyclizations. *Synth. Commun.* **2019**, *49*, 463–481. https://doi.org/10.1080/00397911.2018.1563796.
22. Qadir, T.; Amin, A.; Sharma, P.K.; Jeelani, I.; Abe, H. A review on medicinally important heterocyclic compounds. *Open Med. Chem. J.* **2022**, *16*, e187410452202280. https://doi.org/10.2174/18741045-v16-e2202280.
23. Zhuang, C.; Zhang, W.; Sheng, C.; Zhang, W.; Xing, C.; Miao, Z. Chalcone: A privileged structure in medicinal chemistry. *Chem. Rev.* **2017**, *117*, 7762–7810. https://doi.org/10.1021/acs.chemrev.7b00020.
24. Amslinger, S. The tunable functionality of α,β-unsaturated carbonyl compounds enables their differential application in biological systems. *ChemMedChem* **2010**, *5*, 351–356. https://doi.org/10.1002/cmdc.200900499.
25. Go, M.L.; Wu, X.; Liu, X.L. Chalcones: An update on cytotoxic and chemoprotective properties. *Curr. Med. Chem.* **2005**, *12*, 481–499. https://doi.org/10.2174/0929867053363153.
26. Kolo, A.M.; İpek, E.; Çapan, İ.; Servi, S. Synthesis of heterocyclic-substituted novel hydroxysteroids with regioselective and stereoselective reactions. *J. Heterocycl. Chem.* **2018**, *55*, 492–497. https://doi.org/10.1002/jhet.3070.
27. Dib, H.; Abu-Samha, M.; Younes, K.; Abdelfattah, M.A.O. Evaluating the physicochemical properties–activity relationship and discovering new 1,2-dihydropyridine derivatives as promising inhibitors for PIM1-Kinase: Evidence from principal component analysis, molecular docking, and molecular dynamics studies. *Pharmaceuticals* **2024**, *17*, 880. https://doi.org/10.3390/ph17070880.
28. Daina, A.; Michielin, O.; Zoete, V. SwissADME: A free web tool to evaluate pharmacokinetics, drug-likeness and medicinal chemistry friendliness of small molecules. *Sci. Rep.* **2017**, *7*, 42717. https://doi.org/10.1038/srep42717.
29. Fu, L.; Shi, S.; Yi, J.; Wang, N.; He, Y.; Wu, Z.; Peng, J.; Deng, Y.; Wang, W.; Wu, C.; et al. ADMETlab 3.0: An updated comprehensive online ADMET prediction platform enhanced with broader coverage, improved performance, API functionality and decision support. *Nucleic Acids Res.* **2024**, *52*, W422–W431. https://doi.org/10.1093/nar/gkae236.
30. Banerjee, P.; Eckert, A.O.; Schrey, A.K.; Preissner, R. ProTox-II: A webserver for the prediction of toxicity of chemicals. *Nucleic Acids Res.* **2018**, *46*, W257–W263. https://doi.org/10.1093/nar/gky318.
31. Yadav, V.K. Relative Aromaticity of Pyrrole, Furan, Thiophene and Selenophene, and Their Diels–Alder Stereoselectivity. In *Steric and Stereoelectronic Effects in Organic Chemistry*; Springer: Berlin/Heidelberg, Germany, 2021; pp. 191–216. https://doi.org/10.1007/978-3-030-75622-2_9.
32. Cicenas, J.; Kalyan, K.; Sorokinas, A.; Stankunas, E.; Levy, J.; Meskinyte, I.; Stankevicius, V.; Kaupinis, A.; Valius, M. Roscovitine in cancer and other diseases. *Ann. Transl. Med.* **2015**, *3*, 135. https://doi.org/10.3978/j.issn.2305-5839.2015.03.61.
33. Steinman, R.A.; Robinson, A.R.; Feghali-Bostwick, C.A. Antifibrotic effects of roscovitine in normal and scleroderma fibroblasts. *PLoS ONE* **2012**, *7*, e48560. https://doi.org/10.1371/journal.pone.0048560.
34. Tron, G.C.; Pirali, T.; Billington, R.A.; Canonico, P.L.; Sorba, G.; Genazzani, A.A. Click chemistry reactions in medicinal chemistry: Applications of the 1,3-dipolar cycloaddition between azides and alkynes. *Med. Res. Rev.* **2008**, *28*, 278–308. https://doi.org/10.1002/med.20107.
35. Brik, A.; Alexandratos, J.; Lin, Y.-C.; Elder, J.H.; Olson, A.J.; Wlodawer, A.; Goodsell, D.S.; Wong, C.-H. 1,2,3-Triazole as a peptide surrogate in the rapid synthesis of HIV-1 protease inhibitors. *ChemBioChem* **2005**, *6*, 1167–1169. https://doi.org/10.1002/cbic.200500101.
36. Thirumurugan, P.; Matosiuk, D.; Jozwiak, K. Click chemistry for drug development and diverse chemical–biology applications. *Chem. Rev.* **2013**, *113*, 4905–4979. https://doi.org/10.1021/cr200409f.

37. Bonandi, E.; Christodoulou, M.S.; Fumagalli, G.; Perdicchia, D.; Rastelli, G.; Passarella, D. The 1,2,3-triazole ring as a bioisostere in medicinal chemistry. Drug Discov. *Today* **2017**, *22*, 1572–1581. https://doi.org/10.1016/j.drudis.2017.05.014.
38. Lv, N.; Huang, C.; Huang, H.; Dong, Z.; Chen, X.; Lu, C.; Zhang, Y. Overexpression of glutathione S-transferases in human diseases: Drug targets and therapeutic implications. *Antioxidants* **2023**, *12*, 1970. https://doi.org/10.3390/antiox12111970.

Disclaimer/Publisher's Note: The statements, opinions and data contained in all publications are solely those of the individual author(s) and contributor(s) and not of MDPI and/or the editor(s). MDPI and/or the editor(s) disclaim responsibility for any injury to people or property resulting from any ideas, methods, instructions or products referred to in the content.